© 2018. Published by The Company of Biologists Ltd | Journal of Cell Science (2018) 131, jcs216176. doi:10.1242/jcs.216176

RESEARCH ARTICLE

Adenylyl cyclase A mRNA localized at the back of cells is actively translated in live chemotaxing *Dictyostelium*

Weiye Wang[1], Song Chen[1,2,3], Satarupa Das[1,3], Wolfgang Losert[3] and Carole A. Parent[1,2,3,*]

ABSTRACT

Dictyostelium discoideum cells transport adenylyl cyclase A (ACA)-containing vesicles to the back of polarized cells to relay exogenous cAMP signals during chemotaxis. Fluorescence *in situ* hybridization (FISH) experiments showed that ACA mRNA is also asymmetrically distributed at the back of polarized cells. By using the MS2 bacteriophage system, we now visualize the distribution of ACA mRNA in live chemotaxing cells. We found that the ACA mRNA localization is not dependent on the translation of the protein product and requires multiple cis-acting elements within the ACA-coding sequence. We show that ACA mRNA is associated with actively translating ribosomes and is transported along microtubules towards the back of cells. By monitoring the recovery of ACA–YFP after photobleaching, we observed that local translation of ACA–YFP occurs at the back of cells. These data represent a novel functional role for localized translation in the relay of chemotactic signals during chemotaxis.

KEY WORDS: mRNA, Live imaging, Translation, Cell migration, *Dictyostelium*

INTRODUCTION

Chemotaxis, the ability of cells to migrate towards chemical gradients, is fundamental to a wide array of biological and pathological processes, including wound healing, immune responses and development, as well as arthritis and cancer metastasis. Chemotaxis is also essential for the survival of the social amoeba *Dictyostelium discoideum* (Artemenko et al., 2014). Upon starvation, these cells enter a developmental program that allows them to chemotax and form an aggregate that will differentiate into a multicellular organism, thereby protecting them from harsh environmental conditions. In the early stages of differentiation, as the cells sense a gradient of the chemoattractant 3′,5′-cyclic adenosine monophosphate (cAMP), they polarize and migrate directionally in a head-to-tail fashion to form streams, which dramatically increase their recruitment range (McCann et al., 2010). The molecular mechanism that regulates *Dictyostelium* streaming initiates when cAMP binds to the cAMP receptor 1 (cAR1) – a seven transmembrane G protein-coupled receptor (GPCR). Activation of the receptor leads to the dissociation of the heterotrimeric G proteins into α- and βγ-subunits, and the activation of downstream effectors that regulate cell polarity and directed motility. The activation of the adenylyl cyclase A (ACA), which converts ATP into cAMP, is essential for relaying chemotactic signals in *Dictyostelium* (Kriebel and Parent, 2004). While some of the cAMP synthesized remains inside the cell to activate downstream PKA signaling, most of the cAMP is secreted and acts in a paracrine fashion to recruit neighboring cells (Manahan et al., 2004).

Live-cell imaging of ACA has revealed that it resides in two distinct pools: one is restricted to the plasma membrane, and the other localizes on highly dynamic vesicles that coalesce at the back of polarized cells, and are shed during chemotaxis and streaming. We have shown that the enrichment of ACA at the back of cells is essential for streaming, and proposed that the shedding of ACA-containing vesicles provides a compartment from which cAMP is secreted to act locally, leading to an environment where attractants can be sustained and delivered to neighboring cells (Kriebel et al., 2003, 2008). Interestingly, using fluorescence *in situ* hybridization (FISH) we also showed that the ACA mRNA is asymmetrically distributed at the back of polarized cells (Das et al., 2017) and envisioned that localized ACA mRNA allows the local translation and accumulation of the ACA protein at the back of cells. We reasoned that in starved, chemotaxis-competent *Dictyostelium* cells, localized mRNA translation would provide an energy efficient means to localize proteins because mRNAs can be translated multiple times at their destination. Furthermore, on-site translation of localized mRNA would bypass the requirements for signals to be targeted to the nucleus to initiate transcription, mRNA export, cytoplasmic translation and the subsequent targeting of the protein to the proper cellular site (Buxbaum et al., 2015). In fact, mRNA localization is an evolutionary conserved gene expression regulation mechanism that underlies multiple cellular functions among different organisms (Jung et al., 2014). For example, the preferential accumulation of Ash1 mRNA in daughter cells in the budding yeast *Saccharomyces cerevisiae* controls mating type switching (Long et al., 1997). Localization of Nanos mRNA at the posterior pole of the *Drosophila* embryo during embryogenesis controls embryonic polarity (Gavis and Lehmann, 1992). Finally, the local translation of β-actin mRNA, which localizes to growth cones and axons, is thought to modulate synaptic plasticity that dictates learning and memory formation in the brain (Bassell et al., 1998; Buxbaum et al., 2014; Kaplan et al., 1992), and it has been shown that localized translation is a key determinant of protein localization to protrusions (Mardakheh et al., 2015).

Chemotaxis-competent *Dictyostelium* cells are highly motile, reaching speeds of 20 µm/min, and frequently reorganizing their shape and subcellular compartments as they navigate complex chemotactic gradients (Artemenko et al., 2014). The FISH technique could not provide the high spatio-temporal dynamics required to adequately assess ACA mRNA localization during chemotaxis. However, recent advances in live-cell mRNA imaging have provided an unprecedented view of mRNA dynamics in a

[1]Laboratory of Cellular and Molecular Biology, Center for Cancer Research, NCI, NIH, Bethesda, MD 20892, USA. [2]Department of Pharmacology, Michigan Medicine, Ann Arbor, MI 48109, USA. [3]Institute for Physical Science and Technology, University of Maryland, College Park, MD 20742, USA.

*Author for correspondence (parentc@umich.edu)

C.A.P., 0000-0002-1518-1452

Received 29 January 2018; Accepted 26 March 2018

variety of systems. In particular, the MS2 bacteriophage system (Beach et al., 1999; Bertrand et al., 1998) has been used in *Saccharomyces cerevisiae* (Beach et al., 1999; Bertrand et al., 1998), neurons (Lionnet et al., 2011), *Drosophila melanogaster* embryos (Jaramillo et al., 2008), fibroblasts (Katz et al., 2016) and non-chemotaxing *Dictyostelium discoideum* cells (Chubb et al., 2006; Masaki et al., 2013). We now established an MS2-based live imaging system to visualize mRNA localization in chemotaxing *Dictyostelium* cells, and assessed ACA mRNA localization under various conditions. We found that ACA mRNA localization depends on the cis-acting elements in the coding sequence. Using lattice light-sheet microscopy (LLSM) with fast acquisition speed, we provide direct evidence that ACA mRNA is being transported along microtubules. Finally, we found that the localized ACA mRNA molecules are under active local translation by performing photobleaching experiments. Taken together, our findings identify a novel functional role for localized translation in the relay of chemotactic signals during *Dictyostelium* chemotaxis.

RESULTS

ACA mRNA is localized at the back of polarized live chemotaxing cells

We set out to visualize ACA mRNA distribution in live cells using the MS2 bacteriophage system. The system utilizes the high-affinity interaction between the MS2 bacteriophage viral replicase translational operator (a 19-nucleotide RNA stem loop) and the MS2 coat protein (Bertrand et al., 1998; Chubb et al., 2006; Golding and Cox, 2004; Janicki et al., 2004). We inserted 24 repeats of the MS2 stem loops immediately after the ACA–YFP coding sequence (ACA–YFP–24xMS2). Upon transcription, the MS2 stem loops are transcribed into mRNA and detected with mRFPmars fused to the phage MS2 coat protein (MS2–RFP), meaning that the ACA mRNA transcripts can be readily visualized as red fluorescent spots (Fig. 1A). To acquire images of ACA mRNA in live chemotaxing cells, we monitored cells as they are chemotaxing towards cAMP in an under-agarose assay (Kriebel and Parent, 2009). We acquired diffraction limited confocal time-lapse image slices and generated maximum intensity projection (MIP) movies. As expected, when MS2–RFP is expressed alone in *aca*$^{-}$ cells, we observed a uniform RFP signal with no punctae (Fig. 1D). In contrast, in cells co-expressing MS2–RFP and ACA–YFP–24xMS2, we observed many dynamic RFP spots that appeared to preferentially localized at the back of chemotaxing cells (Fig. 1B,E; Movie 1). As a control for these studies, we co-expressed cAR1–YFP–24xMS2 and MS2–RFP in cells double null for cAR1 and cAR3 (*car1/3*$^{-/-}$). We previously showed that the cAR1 mRNA is uniformly distributed in the cytoplasm of polarized chemotaxing cells (Das et al., 2017). Similarly, we found that the fluorescent signals from the cAR1 mRNA in live chemotaxing cells appeared in random locations across the cells (Fig. 1C,F; Movie 1). To check whether MS2–RFP binds to ACA–YFP–24xMS2 specifically, we performed FISH experiments using fluorescently labeled oligonucleotide probes against ACA mRNA (Das et al., 2017) on cells co-expressing ACA–YFP–24xMS2 and MS2–RFP constructs (Fig. S1A). As expected, we observed colocalization of FISH and MS2 signals in polarized cells (Pearson's coefficient: 0.773).

We next quantified the subcellular distribution of ACA and cAR1 mRNA transcripts in live cells. We quickly realized that our previous algorithm for quantifying the mRNA FISH images in fixed cells (Das et al., 2017) at a single moment was not applicable. A quantification method that could capture the dynamic nature of mRNA localization in highly motile cells was required. We therefore developed a new algorithm to quantify mRNA localization in multiple cells throughout each movie. To calculate the mRNA localization along the longitudinal axis of the cell migration direction, we needed to determine the cell orientation for each frame of the movies. We averaged the turning angles of five successive time points and assigned the result to the center time point as the instantaneous direction of the cell migration (Fig. S1B,C). However, chemotaxing cells frequently reorganize their shape and the relative position of their subcellular compartments. We therefore only quantified the ACA mRNA localization for cells that were migrating in a straight line. To achieve this, all the relative turning angles in each movie were collected and only the frames with turning angles within a mean turning angle $\pm 1\sigma$ (standard deviation) were quantified. Cells from these frames of every movie were aligned along their instantaneous direction, and the cell length was normalized to generate a kymograph with mRNA spots and the nucleus located on the relative scaled positions (Fig. S1D). To calculate the average spatial distribution of mRNA spots throughout all frames for multiple cells, we adapted the pair-correlation function from soft matter physics to the mRNA spots localization. In soft matter physics, the pair-correlation function is a measure of the probability of finding a particle at a distance of r away from a given reference particle (Chen et al., 2006). A general algorithm determines the number of particles [n(r)] between the distances of r and $r+\Delta r$ away from a reference particle. Then the probability is calculated by dividing n(r) by the overall density of particles as if they were uniformly distributed. Inspired by the pair-correlation function, we set the cell nucleus as the origin point (reference particle), with the cell length scaled between −1 (cell front) and +1 (cell back), and determined the fluorescent signals of the mRNA spots between the distances of r and $r+\Delta r$ away from the cell nucleus. The probability of finding mRNA spots (mRNA spatial distribution function, SDF) was calculated by dividing this number by the overall mRNA density as if they were uniformly distributed across the whole cell according to:

$$g(r) = \frac{n(r \sim r + \Delta r)}{\rho\, 2\pi r \Delta r},$$

where

$$\rho = \frac{n(all\ signal)}{cell\ area}.$$

The single-cell SDF was generated for each cell in each movie. The general SDF for each cell line/condition was generated by averaging several (indicated in each figure legend) single-cell SDFs. As shown in Fig. 1G, the peak height correlates with the probability of mRNA shown in each position. The flat line in the front quarter (−1.0∼−0.5) of ACA–YFP–24xMS2/MS2–RFP/*aca*$^{-}$ cells indicates that virtually no ACA mRNA was observed in that area, while peaks in the back quarter (0.5–1.0), especially within the red box (∼0.65–1.0), indicates a much higher probability of mRNA localization compared to our control cAR1-YFP-24xMS2/MS2-RFP/*car1/3*$^{-}$ cells. We also identified a strong perinuclear localization for both the ACA and cAR1 mRNAs as well as several lower localization peaks between the nucleus and the back of the cells, which suggest that the ACA mRNA spots are being transported from the perinuclear area to the back of the cells.

Journal of Cell Science (2018) 131, jcs216176. doi:10.1242/jcs.216176

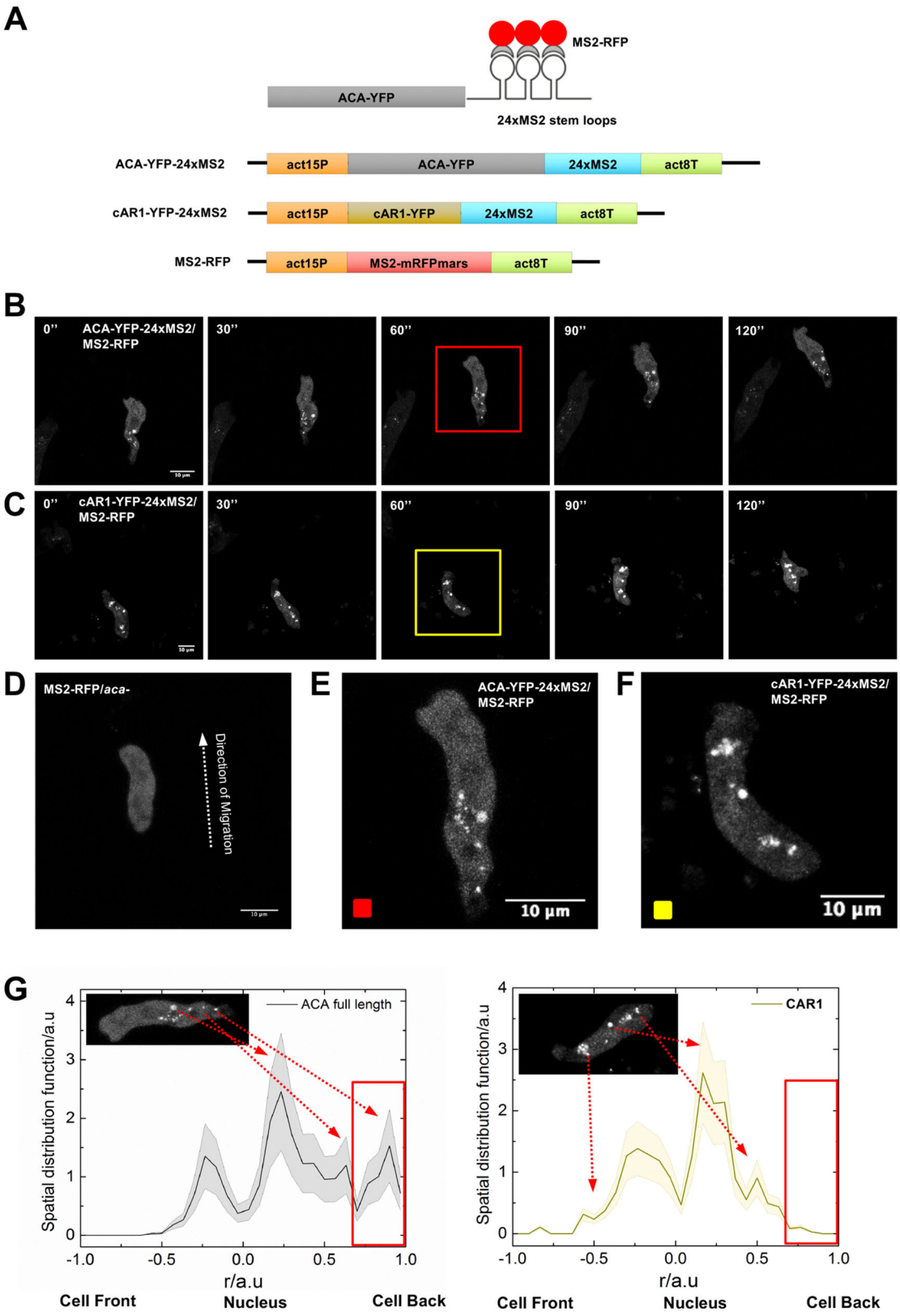

Fig. 1. ACA mRNA imaging in live chemotaxing *Dictyostelium* cells. (A) Schematic representing the MS2-based live RNA imaging system used in this study (act15P, *actin 15* promoter; act8T, *actin 8* terminator). (B,C) Sequential fluorescence maximum intensity projections (MIPs) of an ACA–YFP–24xMS2/MS2–RFP/*aca*$^{-}$ cell (B) and a cAR1–YFP–24xMS2/MS2–RFP/*car1*/*3*$^{-/-}$ cell (C) migrating under agarose towards a cAMP gradient. Also see Movie 1. (D) MIPs of a MS2–RFP/*aca*$^{-}$ cell migrating under agarose towards a cAMP gradient. The arrow indicates the direction of migration. (E,F) Magnified views of the areas highlighted by boxes in B and C. (G) mRNA SDF for ACA–YFP–-24xMS2/MS2–RFP/*aca*$^{-}$ (n=10) and cAR1–YFP–24xMS2/MS2-RFP/*car1*/*3*$^{-/-}$ cells (n=10). Solid lines with shade bands indicate the mean±s.e.m. Red arrows correlate the mRNA spots and SDF peaks. The red box indicates the probability peaks for mRNA localized at the back of the cell.

Journal of Cell Science (2018) 131, jcs216176. doi:10.1242/jcs.216176

The ACA mRNA localization to the back of migrating cells is independent of ACA protein translation

We next asked whether the asymmetric distribution of the ACA mRNA specifically requires the translation of the ACA polypeptide. We generated a fusion construct where the ACA open reading frame (ORF) was fused immediately after the stop codon of the GFP ORF followed by 24 MS2 stem loops (GFP-Stop–ACA–24xMS2) and expressed it in *aca*$^{-}$ cells (Fig. 2A), where no functional ACA protein is made. Cells were allowed to migrate directionally towards cAMP in the under-agarose assay and images were captured every 15 s. As a control for these experiments, we used *aca*$^{-}$ cells expressing the GFP-Stop–24xMS2 (Fig. 2A). As expected, both cell lines showed a uniform cytoplasmic distribution of the GFP protein (Fig. S2A). However, while the GFP-Stop–24xMS2/*aca*$^{-}$ cells showed a uniform distribution of the GFP mRNA, the GFP-Stop–ACA–24xMS2/*aca*$^{-}$ cells showed a strong probability of localized mRNA at the back of migrating cells (Fig. 2B,C; Movie 2). Noticeably, the SDF of GFP-Stop–24xMS2 mRNA, which was similar to that of cAR1–YFP–24xMS2, showed wider peaks compared to the ACA–YFP–24xMS2 and GFP-Stop–ACA–24xMS2 peaks, suggesting that ACA mRNA transportation and localization is under tight spatial regulation towards the cell back. To assess whether the fused GFP-Stop–ACA mRNA transcript was synthesized, we isolated RNA from the GFP-Stop/*aca*$^{-}$ and GFP-Stop–ACA/*aca*$^{-}$ cell lines and performed RT-PCR using primers upstream and downstream of the GFP-Stop–ACA junction. As depicted in Fig. S2B, we observed the expected 396 bp band exclusively in the GFP-Stop–ACA cells.

To gain more insight into this, we studied the cellular distribution of the ACA protein and ACA mRNA in live chemotaxing cells. As our 24xMS2 insert is downstream of ACA-YFP, we could readily visualize both ACA mRNA and ACA-YFP protein simultaneously. As shown in Fig. 2D and Movie 3, we found that the ACA mRNA and the ACA protein do not colocalize in chemotaxing cells (Pearson's co-efficient −0.1199). Taken together, these findings establish that the ACA mRNA localization to the back of chemotaxing cells is not dependent on translation of the protein, and that the ACA mRNA sequence alone is sufficient to localize the ACA transcript to the back of chemotaxing cells.

ACA mRNA localization to the back of chemotaxing cells depends on cis-acting elements

To begin to identify the cis-acting elements that regulate the distribution of the ACA mRNA, we generated three chimeric mRNA constructs harboring ACA mRNA C-terminal deletion mutants followed by 24 MS2 stem loops. Each of the three plasmids was co-expressed with MS2–RFP in *aca*$^{-}$ cells (Fig. 3A). While each construct gave rise to the expected mRNA species (Fig. S3A,B), we found that none of these plasmids rescued the streaming phenotype of *aca*$^{-}$ cells (data not shown), indicating that no functional ACA polypeptide was expressed in these cells. We next performed the under-agarose chemotaxis assay and assessed the mRNA localization in these mutants. We found that all three truncated mRNAs were targeted to the back of chemotaxing cells (Fig. 3B,C; Movie 4) – a finding that also supports our data showing that ACA translation is not required for its mRNA localization (Fig. 2A–C). To narrow down the size of the localization elements present in the ACA coding sequence, we divided the ACA cDNA into four fragments (ACA1–ACA4) and fused them immediately after the stop codon of GFP, followed by the 24xMS2 stem loops (Fig. 3D) – much like we did to assess the requirement of the ACA polypeptide in mRNA transport (Fig. 2). Using the translatable GFP-fused mRNA strategy offered two main advantages: (1) it provided information on both mRNA and protein localization, and (2) it protected the short truncated ACA mRNAs from potential nonsense-mediated decay. GFP-Stop–24xMS2 and GFP-Stop–ACA–24xMS2 served as negative and positive controls for these experiments. The four constructs were expressed in *aca*$^{-}$ cells and showed a uniform cytoplasmic distribution of the GFP protein (Fig. S3C). We found that the mRNAs from the ACA2- and ACA4-expressing cells did not localize to the back of chemotaxing cells and exhibited a distribution pattern similar to that seen in the cAR1–YFP–24xMS2 cells (Fig. 3E,F and Fig. 1C,F,G; also see Movie 5). In contrast, and in accordance with the findings with the C-terminal deletion mutants (Fig. 3B,C) that harbor part of the ACA1 and ACA3 sequences, cells expressing the ACA1 and ACA3 constructs showed a strong distribution to the back of cells that was comparable to that seen in ACA–YFP–24xMS2 cells (Figs 3E,F and Fig. 1B,E, G; also see Movie 5). From these findings, it therefore appears that multiple cis-acting elements are present in the ACA-coding sequence, and that each element is sufficient, but not essential, to target the ACA mRNA at the back of chemotaxing cells.

ACA mRNA is actively transported along microtubules

The cytoskeleton has been shown to play an important role in regulating mRNA localization in various organisms (Jeffery, 1985; Litman et al., 1994; Pondel and King, 1988; Sundell and Singer, 1991; Yisraeli et al., 1990). We first investigated the function of the microtubule network in ACA mRNA transport. We generated cells co-expressing GFP-tagged tubulin A (GFP–TubA), MS2–RFP and ACA–24xMS2 (Fig. 4A). To capture the high spatio-temporal dynamics of the ACA mRNA and the microtubule network in three dimensions (3D), we used LLSM (Chen et al., 2014). With the high *z*-axis resolution of LLSM, we were able to optically section live cells densely along the *z*-axis and resliced them to obtain a *yz* view. As shown in Fig. 4B, we found that the ACA mRNA spots are closely associated with the microtubule network, which emanates toward the back of cells (Fig. 4B, zoom in box and *yz* views, see Fig. 4C for more examples). We also found that the lamellipodia at the front of polarized cells is devoid of ACA mRNA spots and microtubules, and that the large perinuclear mRNA spots are closely associated with the microtubule-organizing center (MTOC) (Fig. 4B, arrow #4, see Fig. 4C for more examples, also see Movie 6). However, because of the highly dynamic nature of the ACA mRNA spots in chemotaxing cells, even the shortest acquisition time for each stack on the LLSM (4.2 secs) could not allow us to track each spot using nearest-neighbor algorithms.

We then treated the cells with 15 µM nocodazole (Noco) for 30 min and monitored the distribution of ACA mRNA spots. Under these conditions, the microtubule network was substantially disassembled (Fig. 5A; Movie 7) and, although the cells could still chemotax, they lost the ability to stream (Movie 7), as previously reported (Kriebel et al., 2008). Under these conditions, we observed a dominant large ACA mRNA spot near the MTOC, which represents the perinuclear population observed in Fig. 1B,E, as well as a few very small ACA mRNA spots located at the back of cells (Fig. 5A; Movie 7). However, we did not observe any ACA mRNA spots between the perinuclear area and the cell back, indicating that ACA mRNA spots being transported along the microtubules are abolished under Noco treatment. We speculate that the small mRNA spots localized at the back were transported and anchored to the cell periphery and released from the microtubule network before Noco treatment. In this context, studies in *Drosophila* oocytes have shown that *nanos* and *oskar* mRNAs are

Journal of Cell Science (2018) 131, jcs216176. doi:10.1242/jcs.216176

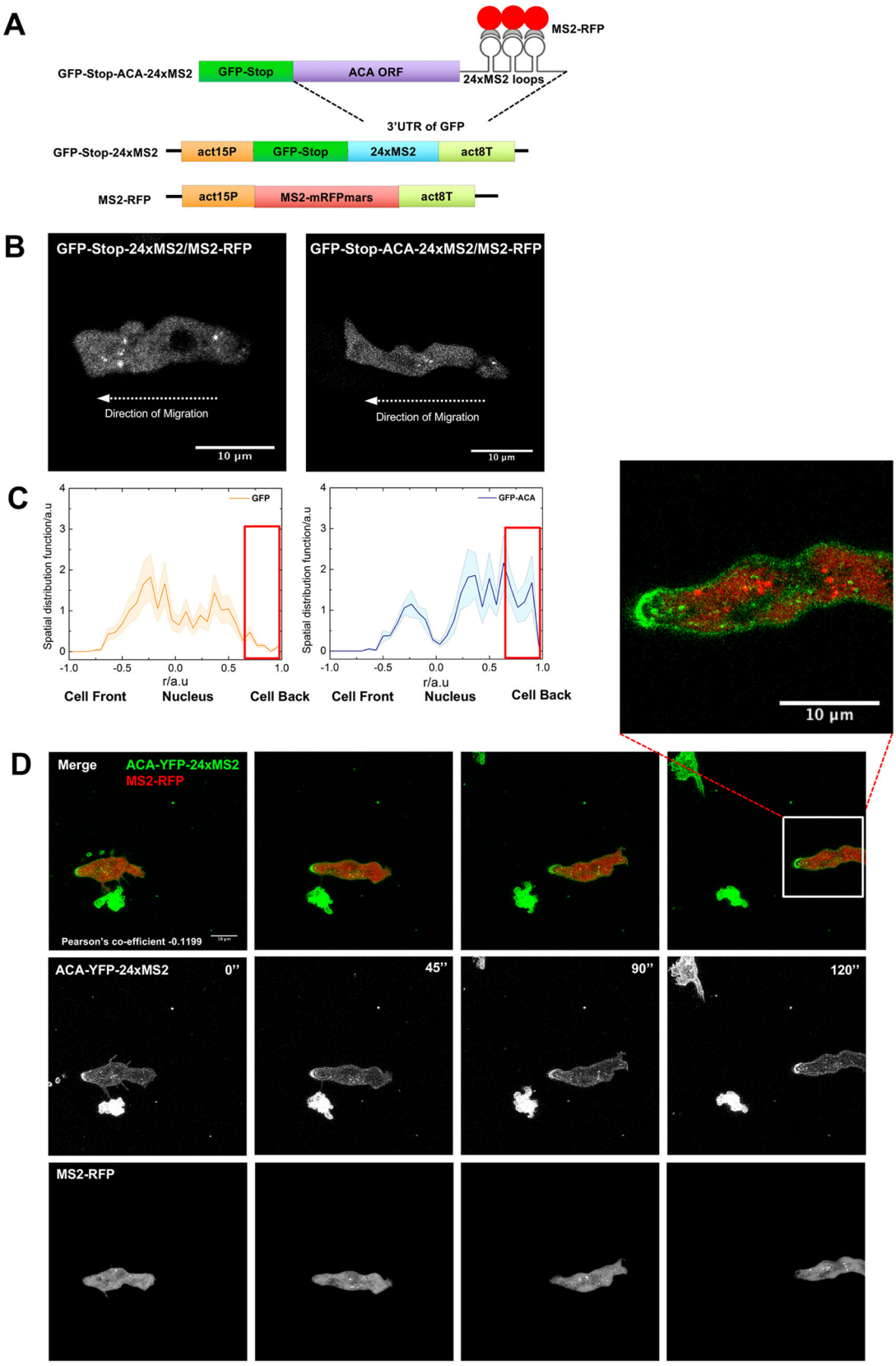

Fig. 2. ACA mRNA localization at the back of chemotaxing cells is independent of the ACA protein. (A) Schematic representing the fusion constructs used in this study. (B) MIPs of a GFP-Stop–ACA–24xMS2/MS2–RFP/*aca*$^{-}$ and a GFP–24xMS2/MS2–RFP/*aca*$^{-}$ cell migrating under agarose towards a cAMP gradient. The arrow indicates the direction of migration. (C) mRNA SDF for GFP–24xMS2/MS2–RFP/*aca*$^{-}$ (*n*=10, abbreviated as 'GFP') and GFP-Stop–ACA–24xMS2/MS2–RFP/*aca*$^{-}$ cells (*n*=11, abbreviated as 'GFP-ACA'). Solid lines with shade bands indicate mean±s.e.m. The red box indicates the probability peaks for mRNA localized at the back of the cell. (D) Sequential fluorescent MIPs of an ACA–YFP–24xMS2/MS2–RFP/*aca*$^{-}$ cell migrating under agarose towards a cAMP gradient (green, ACA–YFP; red, MS2–RFP). Also see Movie 2.

Journal of Cell Science (2018) 131, jcs216176. doi:10.1242/jcs.216176

anchored in the posterior area in an actin-dependent manner (Forrest and Gavis, 2003). In fibroblasts, β-actin mRNA is also linked to actin filaments via the translational machinery (Liu et al., 2002).

We next studied the role of the actin cytoskeleton on ACA mRNA transport. For these experiments, we treated cells with 5 µM Latrunculin A (LatA) for 30 min and monitored the ACA mRNA localization. As previously reported, we found that upon LatA treatment cells rapidly lose polarity and stop moving (Kriebel et al., 2008). Under these conditions, the ACA mRNA spots appeared to be randomly localized (Fig. 5B, also see Movie 7). However, unlike the Noco-treated cells, LatA-treated cells still had a significant amount of ACA mRNA spots that were associated with and rapidly moving along the intact highly dynamic microtubule network (Fig. 5B, arrows, Movie 7). To further substantiate our findings, we performed washout experiments on Noco- or LatA-treated cells and monitored the dynamics of ACA mRNA and microtubules. As shown in Fig. 5C, the ACA mRNA spots withdrew to the MTOC area under Noco treatment. However, as early as 5 min after Noco washout, the microtubule network was re-established, the cells regained polarity, and the asymmetric distribution of ACA mRNA was readily observed at the 10 min time point. Similarly, upon LatA washout, the cells slowly regained polarity, the ability to migrate and ACA mRNA asymmetry (Fig. 5D). Taken together, these findings indicate that the ACA mRNA spots associate with microtubules and localize to the back of polarized cells and that the actin cytoskeleton is not critically involved in this process.

Kinesins and dyneins are large motor complexes that move along microtubules toward different destinations and mediate a variety of cellular processes within eukaryotic cells (Hirokawa et al., 2009; Vallee et al., 2004). Thirteen kinesins have been identified in the *Dictyostelium* genome (Kollmar and Glockner, 2003). However, the lack of specific inhibitors and the redundancy of the *Dictyostelium* kinesin family make it extremely challenging to study the role of kinesins in *Dictyostelium* mRNA transport. The *Dictyostelium* cytoplasmic dynein is a single large motor complex that powers cellular motility through the coordinated action of a number of subunits of the dynein complex (Koonce et al., 1992). In fact, this minus-end-directed microtubule motor complex has been reported as a key player in mRNA transport in various organisms (Vallee et al., 2004). We therefore set out to determine the role of dynein in ACA mRNA transport by treating cells with Ciliobrevin D (CilD), a specific small-molecule antagonist of cytoplasmic dynein (Firestone et al., 2012). In these experiments, we treated ACA–24xMS2/MS2–RFP/GFP–TubA/*aca*$^{-}$ cells with 40 µM CilD for 30 min and first assessed the migration ability of the cells. We found that CilD treatment decreased the speed of cell movement (Fig. S4C, Movie 8), without disturbing the integrity of the microtubule network (Fig. 5E, left panel; Movie 9). CilD-treated cells were able to maintain polarity and migrate directionally towards a cAMP gradient, but exhibited significant streaming defects (Fig. SA,B,D, Movie 8). Indeed, we found that the asymmetric ACA mRNA distribution at the back of cells was lost in CilD-treated cells, and that the non-MTOC associated mRNA spots showed an increased probability to associate with the microtubules in front of the nucleus (Fig. 5E,F; Movie 9). We also found that CilD-treated cells showed broader mRNA distribution peaks (Fig. 5F) compared to that of ACA–YFP–24xMS2/MS2–RFP/*aca*$^{-}$ cells, similar to what we observed for cAR1–YFP–24xMS2 and GFP–24xMS2 mRNAs. These findings show that while dynein does not regulate chemotaxis and migration, it does impact cell speed and, most noticeably, it regulates ACA mRNA transport and streaming.

ACA is actively translated at the back of chemotaxis-competent cells

We next set out to measure ACA translation. We first measured the extent to which ACA is actively translated in chemotaxis-competent cells. For this purpose, we determined whether ACA mRNA is associated with actively translating ribosomes. We adopted the ribopuromycylation method used by David et al. (David et al., 2012) to immobilize "puromycylated" nascent chains on ribosomes in the presence of the chain elongation inhibitors puromycin (PMY) and emetine. We observed high amounts of 'puromycylated' nascent protein chains in both WT and ACA–YFP/*aca*$^{-}$ cells (Fig. 6A, top panel). The nascent chains bound to the ribosomes were immunoprecipitated with the anti-PMY antibody and blotted for rpl8 – a large ribosomal protein (David et al., 2013, 2012). We found immunoprecipitated PMY-tethered actively translating ribosome complexes in both WT and ACA–YFP/*aca*$^{-}$ cells, although we routinely observed a much stronger signal in ACA–YFP/*aca*$^{-}$ cells (Fig. 6A, middle panel). Remarkably, RT-PCR analysis of the dissociated complex further revealed that ACA mRNA, but not cAR1 mRNA, is associated with actively translating ribosomes (Fig. 6A, bottom panels; *carA*, gene name of cAR1). These findings are not surprising as we previously showed that (Kriebel et al., 2008), in contrast to ACA–YFP, the expression level of cAR1–YFP is not altered after a 2 h cycloheximide treatment in chemotaxis-competent cells. Moreover, while we measured minimal cAR1–YFP ^{35}S-methionine/cysteine incorporation in differentiated cells, incorporation in ACA–YFP was rapid and robust following cAMP stimulation (Kriebel et al., 2008).

To investigate whether the ACA mRNA localized at the back is being translated and contributes to the enrichment of the ACA protein at the back of chemotaxing cells, we performed photobleaching experiments to monitor ACA translation in real time. By using fluorescence recovery after photobleaching (FRAP), we previously showed that the enrichment of ACA–YFP at the back of migrating cells recovers within 5 min after bleaching in a cycloheximide-dependent manner, indicating that the enrichment is due to *de novo* protein synthesis (Kriebel et al., 2008). We now aimed to measure the recovery kinetics of newly synthesized ACA–YFP in distinct cellular pools in highly polarized cells. Using whole-cell FRAP, we found that the recovery specifically appears at the back of cells, reaching 41% of the initial fluorescence value 10 min after photobleaching (Fig. 6B). Indeed, the ACA–YFP recovery in the central perinuclear area or at the side of cells did not exceed the spontaneous fluorescence recovery of YFP measured in fixed samples (Fig. 6B,F). Similarly, cAR1–YFP recovery did not surpass the spontaneous recovery of YFP in fixed samples (Fig. 6F). Not surprisingly, we found that treatment with 50 µg/ml PMY for 40 min dramatically decreased the fluorescence recovery in all three compartments of the cells (Fig. 6C). However, PMY-treated cells were able to maintain ACA mRNA localization at their back (Fig. S5). The rapid and robust recovery of ACA–YFP at the back of cells could be due to mechanisms other than local *de novo* synthesis of ACA. Active ACA–YFP protein transport could be involved, as we previously showed that ACA–YFP-containing vesicles are actively transported along microtubules towards the back of cells (Kriebel et al., 2008). Furthermore, YFP maturation from existing non-matured fluorescent proteins at the time of photobleaching could also contribute to the recovery we are measuring. To further investigate this, we pre-treated ACA–YFP/*aca*$^{-}$ cells with 50 µg/ml PMY for 40 min, which blocked all active translation and allowed enough time for all existing YFP molecules to mature. We then washed-out PMY and treated cells with 15 µM Noco to block both

Journal of Cell Science (2018) 131, jcs216176. doi:10.1242/jcs.216176

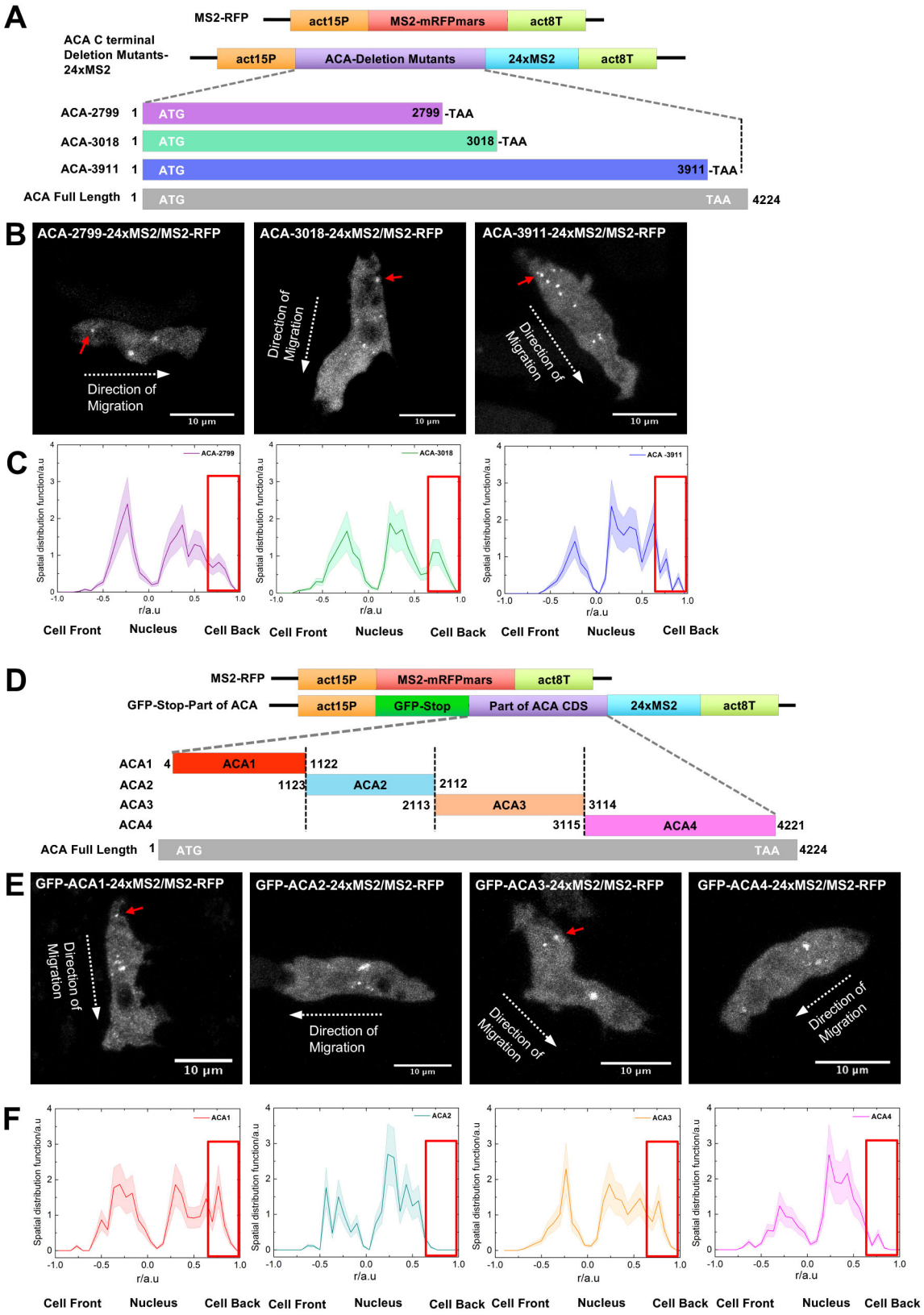

Fig. 3. See next page for legend.

ACA protein and mRNA transport. FRAP experiments were performed on these cells to monitor on-site translation of ACA mRNA that is anchored at the back of the cells. We measured a significantly higher fluorescence recovery at the back of the PMY-washout Noco-treated cells (27%) compared to the PMY-treated cells (20%) (Fig. 6D,E). We attribute the difference between these two back-localization recoveries (Fig. 6E, blue and green lines) to the active translation of the anchored ACA mRNA at the back of

Journal of Cell Science (2018) 131, jcs216176. doi:10.1242/jcs.216176

Fig. 3. The ACA1 and ACA3 regions within the ACA-coding sequence harbor cis-acting elements that localize ACA mRNA to the back of cells. (A) Schematic representing the C-terminal deletion mutants used in this study. (B) MIPs of ACA-2799–24xMS2/MS2–RFP/*aca*$^{-}$, ACA-3018–24xMS2/MS2–RFP/*aca*$^{-}$ and ACA-3911–24xMS2/MS2–RFP/*aca*$^{-}$ cells migrating under agarose towards a cAMP gradient. White arrows indicate the direction of migration. Red arrows indicate the mRNA localized at the back of the cell. (C) mRNA SDF for ACA-2799–24xMS2/MS2–RFP/*aca*$^{-}$ (n=11), ACA-3018–24xMS2/MS2–RFP/*aca*$^{-}$ (n=10) and ACA-3911–24xMS2/MS2–RFP/*aca*$^{-}$ (n=11) cells. Solid lines with shade bands indicate mean±s.e.m. Red boxes indicate the probability peaks for mRNA localized at the back of the cell. (D) Scheme representing the chimeric GFP–ACA1∼4–24xMS2 fusion mRNA to determine the cis-acting elements for ACA mRNA localization. (E) MIPs of GFP–ACA1∼4–24xMS2/MS2–RFP/*aca*$^{-}$ cells migrating under agarose towards a cAMP gradient. White arrows indicate the direction of migration. Red arrows indicate the mRNA localized at the back of the cell. (F) mRNA SDF for GFP–ACA1∼4–24xMS2/MS2–RFP/*aca*$^{-}$ cells (ACA1, n=10; ACA2, n=10; ACA3, n=10; ACA4, n=10). Solid lines with shade bands indicate mean±s.e.m. Red boxes indicate the probability peaks for mRNA localized at the back of the cell.

cells (see Fig. 5A). The difference between the back-localization recovery of non-treated (41%) and PMY-washout cells (27%) (Fig. 6E, red and blue lines) may be due to protein and mRNA transport and YFP maturation. Since ACA is a transmembrane protein and its translation is likely to associate with the secretory pathway, we stained ACA–YFP/*aca*$^{-}$ cells with calnexin, an endoplasmic reticulum (ER) marker (Muller-Taubenberger et al., 2001; Garcia et al., 2009). As shown in Fig. S6, we found that the ER is widely distributed throughout the cell body and the back of cells, which provides the base for local ACA mRNA translation. Taken together, these findings show that the ACA–YFP mRNA localized at the cell back of cells is actively translated.

DISCUSSION

We previously showed that the ACA mRNA asymmetrically localizes to the back of chemotaxing cells by using FISH (Das et al., 2017). However, the FISH procedure involved multiple steps of chemical treatments and prevented us from understanding the spatio-temporal dynamics of ACA mRNA in chemotaxing cells. To assess how ACA mRNA localization is regulated in real time, here, we took advantage of the MS2-based imaging system in live chemotaxing *Dictyostelium* cells and developed a quantification method to assess the dynamics of the ACA mRNA localization. Our findings reveal the dynamics of ACA mRNA localization at the back of live chemotaxing cells. We show that this is determined by cis-acting elements residing in distinct coding sequences, and that the localization is independent of the translation of the protein product. By performing LLSM, we further show that microtubules are required to transport the ACA mRNA towards the back of cells and that dynein regulates the ACA mRNA transport along the microtubules. Finally, using ribopuromycylation and FRAP assays, we show that the ACA mRNA is actively and spatially translated in chemotactic cells. Our findings therefore present a functional role for mRNA localization during the relay of chemotactic signals in amoeboid cells, where the maintenance of localized protein expression is necessary to allow for fast spatio-temporal events to occur, and provide new insight into the mechanisms that regulate such events.

By visualizing the appearance of ACA protein and mRNA after translational block, we previously showed that newly synthesized ACA protein and mRNA reappear and localize to the back of cells as they become polarized (Das et al., 2017; Kriebel et al., 2003, 2008). We now show that the ACA ORF, when fused after the stop codon of GFP, targets the GFP mRNA to the back of chemotaxing cells. This finding established that the localized distribution of the ACA mRNA does not rely on its translational product. In other words, the ORF of ACA mRNA is sufficient to drive its localization to the back of cells in the absence of the ACA polypeptide. Indeed, we found that none of the mRNA spots colocalize with the ACA–YFP-containing vesicles. We previously showed that constructs harboring the 3′ end of ACA mRNA (2364–4224 bp) specifically localize to the back of chemotaxing cells, while constructs harboring the 5′ (1–2363 bp) accumulate in the perinuclear region (Das et al., 2017). We now extended these findings using our live system, and uncovered that multiple cis-acting elements are required to localize the ACA mRNA to the back of cells. We found that constructs harboring shorter regions of both the 5′ and 3′ parts of the ACA coding sequence can localize to the back of chemotaxing cells. Remarkably, ACA1 (4–1122 bp), which is shorter than the 5′ end mutant (1–2363 bp), localized to the back of cells, while the 5′ end construct did not. We reason that the fusion of translatable GFP mRNA in front of the ACA1 sequence helps stabilize the GFP–ACA1 mRNA, while the 5′ end mutant (1–2363 bp), which cannot be translated into a functional protein, is subject to nonsense-mediated mRNA degradation. The ACA3 region (2113–3114 bp) of the coding sequence overlaps with the 3′ end mutant mRNA (2364–4224 bp). We propose that the cis-acting elements, which localize ACA mRNA, reside in the ACA1 (4–1122 bp) and ACA3-3′ overlapping (2364–3114 bp) regions. In fact, multiple cis-acting elements have been found in mRNA-coding regions from other organisms, such as E1, E2A and E2B in ASH1 from *Saccharomyces cerevisiae* (Chartrand et al., 1999). Moreover, a recent study has shown that mRNAs coding for key components of the *Dictyostelium* chemotaxis signaling machinery are distributed at the front of polarized cells in a Pumilio-dependent manner (Hotz and Nelson, 2017). Not surprisingly, because ACA is not required for chemotaxis (Kriebel et al., 2003), we did not identify Pumilio-binding sequences within the ACA coding sequence. Future studies will focus on identifying RNA-binding proteins that interact with ACA mRNA.

Active, motor-based locomotion of mRNAs has been shown in various cell types across different model organisms (Buxbaum et al., 2015). In fact, it has been shown that molecular motor-mediated mRNA transport is much more efficient than passive diffusion (Fusco et al., 2003). However, how *Dictyostelium* transport mRNAs is largely unknown. The LLSM provided a powerful tool to visualize the dynamic interplay between ACA mRNA and microtubules, as we could clearly observe that the ACA mRNA closely associates with microtubules. We also observed that the ACA mRNA spots near the nucleus are closely associated with the MTOC, and our SDF plots show that these MTOC-associated mRNA spots correlate with high-probability peaks close to the nucleus (the peak height behind the nucleus was ∼2.5 a.u versus 1.5 a.u. in front of the nucleus) (Fig. 1G). The ratio between these peaks translates to a 62.5% [2.5/(2.5+1.5)] probability of finding the mRNA spots behind the nucleus. These results echo our previous findings showing that in 62% of migrating cells, the MTOC is localized behind the nucleus where an intricate microtubule network emanates toward the back of cells (Kriebel et al., 2008). Remarkably, we found that ACA mRNA spots withdrew to the MTOC under Noco treatment. Studies in *Drosophila* have shown that dynein and kinesin regulate the dynamics of stress granules (Loschi et al., 2009), which form from stress-induced translational silenced mRNA granules. These stress granules contain mRNAs stalled in translation initiation, various translation initiation factors,

Journal of Cell Science (2018) 131, jcs216176. doi:10.1242/jcs.216176

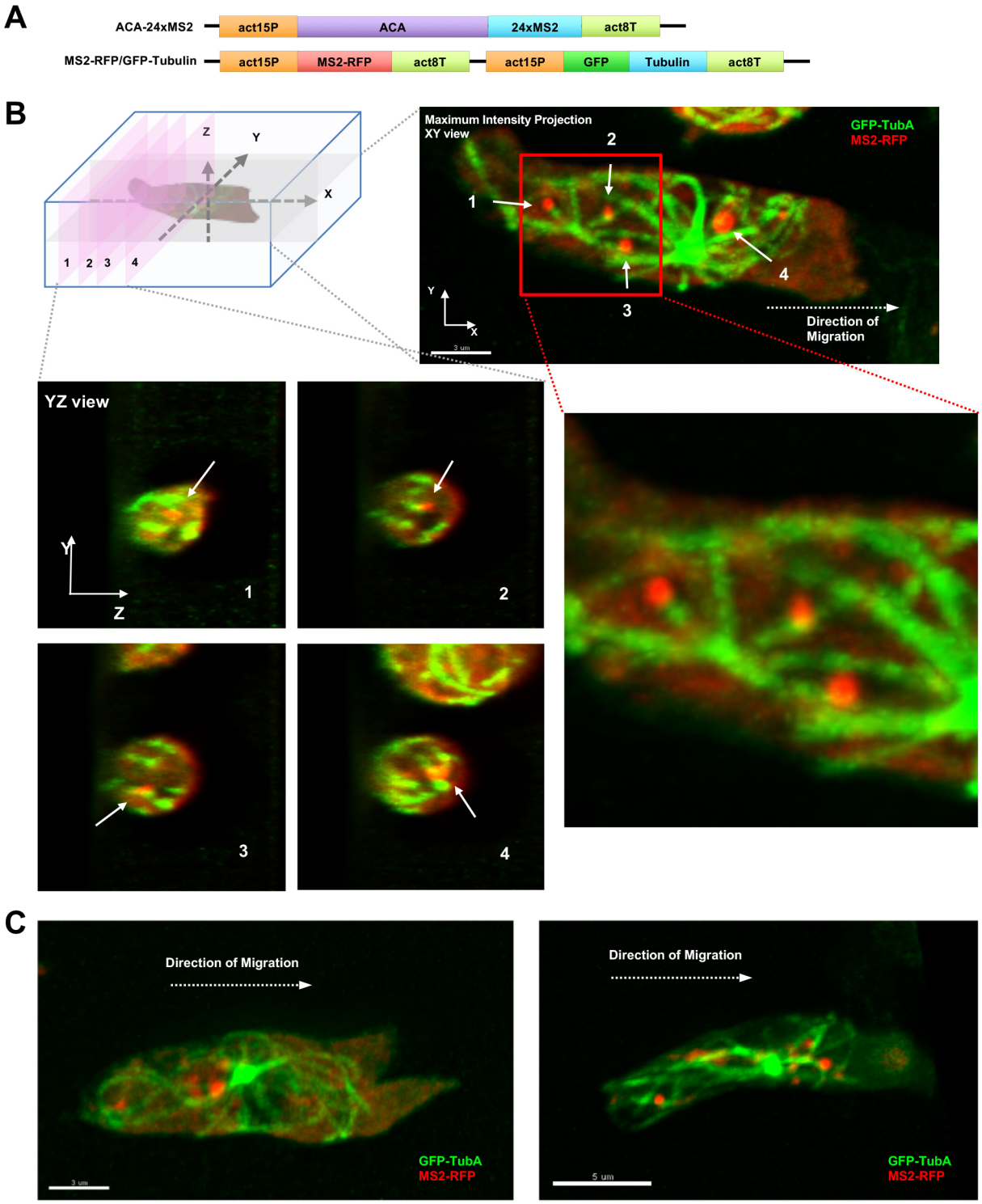

Fig. 4. The ACA mRNA is transported along microtubules to the back of migrating cells. (A) Schematic representing the constructs used for the study. (B) Top left panel, cartoon depicting the 3D projection methods used in this study. Top right panel, MIP of ACA–24xMS2/MS2–RFP/GFP–TubA/*aca*$^{-}$ cells acquired by LLSM. The dashed white arrow indicates the migration direction. Solid numbered arrows indicate the mRNA spots (green, GFP–TubA; red, MS2–RFP). Lower left panels. *yz* view of the four numbered spots shown in the top right panel. Bottom right panel, magnified images of the area highlighted by the red box in the top right panel. (C) MIP of ACA–24xMS2/MS2–RFP/GFP–TubA/*aca*$^{-}$ cells acquired by LLSM. The dashed white arrows indicate the migration direction (green, GFP–TubA; red, MS2–RFP).

a variety of RNA-binding proteins and many non-RNA-binding proteins, and are thought to function as an mRNA-protective and -sorting center (Decker and Parker, 2012; Kedersha et al., 2000; Mollet et al., 2008). It is thought that the sequestered mRNAs in stress granules are delivered to specific sites in the cell for later activation (Anderson and Kedersha, 2009). Interestingly, the size of the ACA mRNA spots near the MTOC is in the range of the size of normal stress granules (0.5–10 µm) (Loschi et al., 2009). We

Journal of Cell Science (2018) 131, jcs216176. doi:10.1242/jcs.216176

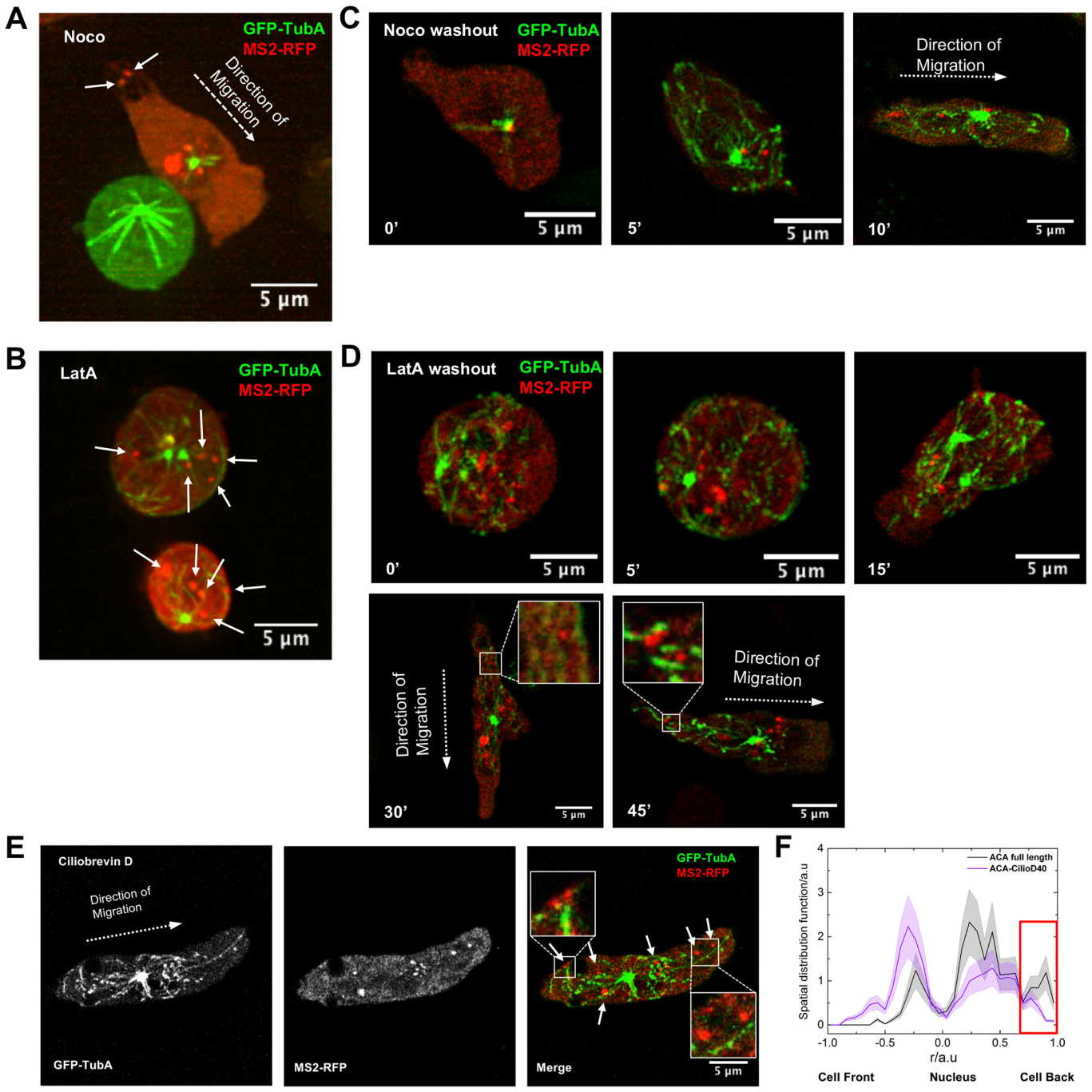

Fig. 5. Dynein and microtubules mediate the ACA mRNA transport towards the back of migrating cells. (A,C) MIPs of ACA–24xMS2/MS2–RFP/GFP–TubA/*aca*$^{-}$ cells treated with 15 µM Noco or 5 µM LatA acquired by LLSM (green, GFP–TubA; red, MS2–RFP). (B,D) Sequential MIPs of ACA mRNA localization in ACA–24xMS2/MS2–RFP/GFP–TubA/*aca*$^{-}$ cells after being treated with 15 µM Noco or 5 µM LatA for 30 min, which was then washed out (green, GFP–TubA; red, MS2–RFP). (E) MIPs of ACA–24xMS2/MS2–RFP/GFP–TubA/*aca*$^{-}$ cells treated with 40 µM CilD (green, GFP–TubA; red, MS2–RFP). In A–E, the dashed white arrows indicate the migration direction, and solid white arrows indicate ACA mRNA spots. (F) mRNA SDF for ACA–24xMS2/MS2–RFP/GFP–TubA/*aca*$^{-}$ cells treated with 40 µM CilD (n=13) (CilD treated, purple line; non-treated, gray line, which is the same as shown in Fig. 1G). Solid lines with shade bands indicate mean±s.e.m.

speculate that starving *Dictyostelium* cells are susceptible to forming stress granules, and that these collect untranslated ACA mRNA to regulate ACA gene expression in a spatiotemporal fashion.

Our ribopuromycylation assay established that the ACA mRNA is actively translated in chemotaxing cells, while the cAR1 mRNA is not. However, imaging exactly where ACA translation occurs in live cells presents a significant challenge. Recent advancements in microscopy methods that use a coat protein knock-off biosensor have identified single mRNAs that were never engaged in translation (Halstead et al., 2015), but this method does not provide information on translation itself. The SunTag system utilizes a repeated peptide array as a protein scaffold that recruits up to 24 copies of a fluorescent protein–fusion antibody (Tanenbaum

Journal of Cell Science (2018) 131, jcs216176. doi:10.1242/jcs.216176

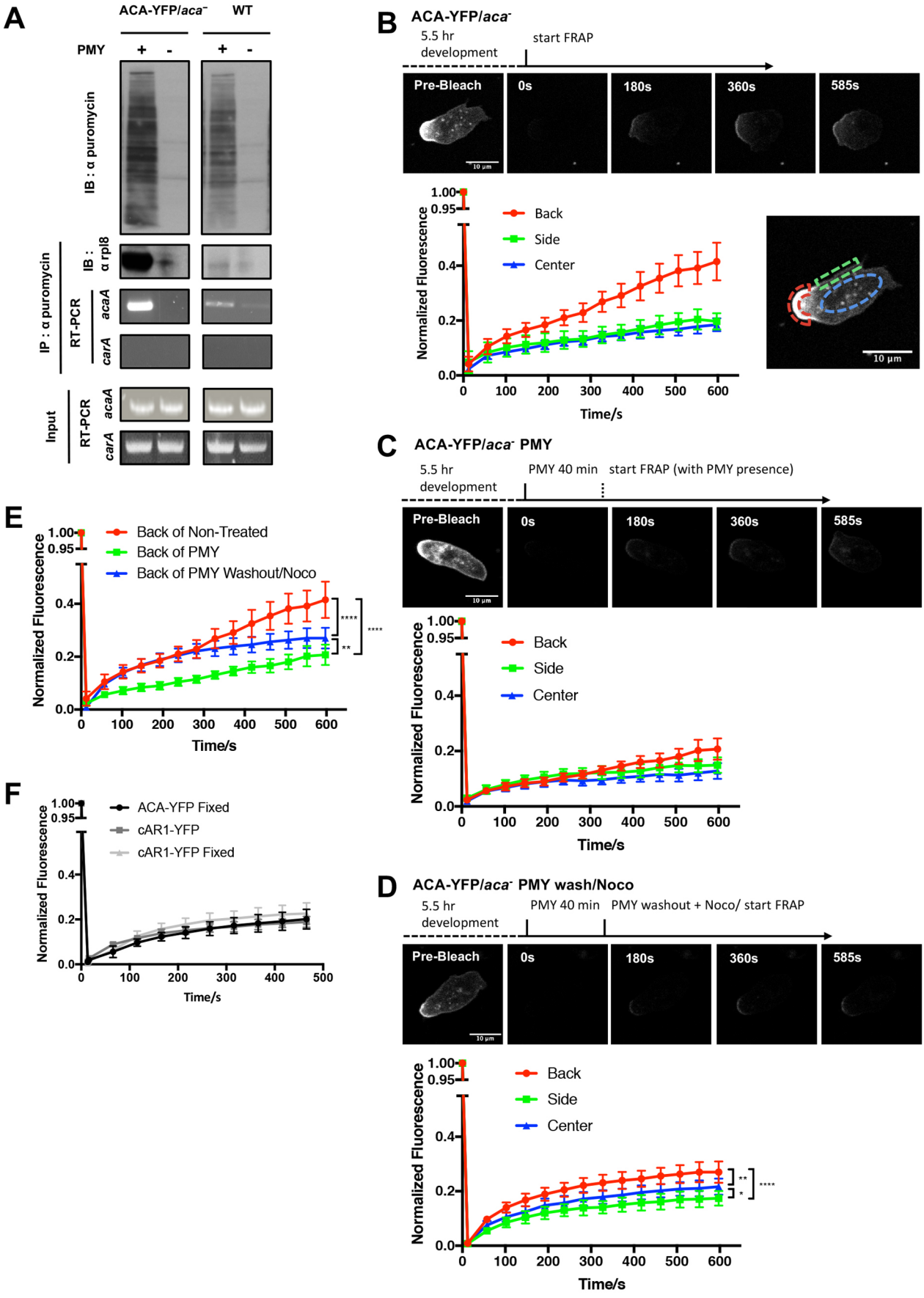

Fig. 6. See next page for legend.

Journal of Cell Science (2018) 131, jcs216176. doi:10.1242/jcs.216176

Fig. 6. ACA is actively translated at the back of chemotaxis-competent cells. (A) Top panel, western blot (IB) analysis of C-terminally puromycylated nascent chains released from ribosomes with and without PMY treatment in ACA–YFP/*aca*$^-$ and WT cells. Middle panels, the complex was immunoprecipitated (IP) using the anti-PMY monoclonal antibody 12D10 and immunoblotted with the anti-rpL8 polyclonal antibody to detect associated ribosomes. The associated RNAs were dissociated from the complex and the presence of mRNAs corresponding to *acaA* (gene name of ACA) and *carA* (gene name of cAR1) were detected by RT-PCR using specific primers. Bottom panels, the presence of *acaA*, *carA* and actin mRNA in the input cell lysates. Data are representative of at least four independent experiments. (B) Top panel, representative confocal fluorescence images of ACA–YFP/*aca*$^-$ cells before and after a complete bleach. The numbers represent the time after the bleach. Bottom panel, total fluorescence recovery of ACA–YFP at the back, center and side of cells as depicted. Results are shown as mean±95% c.i. (*n*=14). (C) Top panel, representative confocal fluorescence images of ACA–YFP/*aca*$^-$ cells treated with 50 µg/ml PMY for 40 min before and after a complete bleach. The numbers represent the time after the bleach. Bottom panel, total fluorescence recovery of ACA–YFP at the back, center and side of cells as depicted in B. Results are shown as mean±95% c.i. (*n*=14). (D) Top panel, representative confocal fluorescence images of ACA-YFP/*aca*$^-$ cells treated with 50 µg/ml PMY for 40 min and then washout PMY followed with 15 µM Noco treatment before and after a complete bleach. The numbers represent the time after the bleach. Bottom panel, total fluorescence recovery of ACA–YFP at the back, center and side of cells as depicted in B. Results are shown as the mean±95% c.i. (*n*=12). **P*=0.0209, ***P*=0.0021, *****P*<0.0001 (two-way ANOVA test). (E) Fluorescence recovery of ACA–YFP at the back of cells as determined from the graphs shown in B–D as indicated. Results are shown as mean±95% c.i. ***P*=0.0082, *****P*<0.0001 (two-way ANOVA test). (F) Total fluorescence recovery of cAR1–YFP over the entire cell for live and fixed samples as indicated. In addition, the spontaneous fluorescence recovery of ACA–YFP in fixed ACA-YFP/*aca*$^-$ cells is presented. Results are shown as mean±95% c.i. (ACA–YFP fixed, *n*=12; cAR1–YFP, *n*=7; cAR1–YFP fixed, *n*=7).

et al., 2014). However, the system creates a ∼1.4 mDa complex that slows down membrane protein diffusion. Furthermore, N-terminus tags of the peptide epitopes will interfere in the translation of membrane protein such as ACA. Biarsenical dyes, FlAsH and ReAsH, which become fluorescent when bound by a peptide that contains four cysteine residues (Zhang et al., 2002) have been used to help determine the location of β-actin translation in C2C12 myoblasts (Rodriguez et al., 2006). Unfortunately, we found these dyes to be toxic to chemotaxis-competent *Dictyostelium* cells (data not shown). FRAP has been widely used to visualize newly synthesized proteins, and does not require extensive tags or treatments. Our FRAP assays established that ACA is locally translated in chemotaxis-competent cells. By using PMY washout and Noco treatment, we were able to assess the extent by which ACA translation occurs at the back of cells. Indeed, the PMY pretreatment allowed enough time for all existing YFP molecules to mature, and the subsequent PMY washout and Noco treatment blocked ACA protein and mRNA transport to the back of cells. In fact, our findings showing that ACA is actively translated at the back of chemotaxing cells are consistent with previous results (Kriebel et al., 2008), which used [^{35}S]methionine/cysteine labeling and showed that rapid and robust ACA–YFP translation occurs as early as 3.75 min after chemotactic stimulation. We propose that the small ACA mRNA spots that remain at the back of cells under Noco treatment are actively being translated. However, it is impossible to visualize these mRNA localized at the back of the cell in FRAP experiments as the bleaching lasers also bleach the MS2–RFP. Nevertheless, from our data, we know that the total fluorescence recovery at 600 s at the back of cells is 21% (Fig. 6E, difference between red line, ∼41%, and green line, ∼20%) and that local translation contributes to 7% of this recovery at the back of cells (Fig. 6E, difference between blue line, ∼27%, and green line, ∼20%), which is nearly one-third (7/21) of the total fluorescence recovery. By using Monte Carlo simulation to estimate the mRNA units, we calculated that ∼10% of ACA mRNA is localized at the back. Studies in *Drosophila* embryo have also shown that only 4% of all *nanos* mRNA and only 18% of all *oskar* mRNA are localized to the posterior pole (Bergsten and Gavis, 1999). Consequently, the 10% localized ACA mRNA contributes to about one-third of the ACA protein at the back, which could provide a redundant mechanism for the enrichment of ACA proteins at the back of chemotaxing cells. It therefore appears that most of the non-localized mRNA molecules are translationally silent. In fact, transported mRNAs, such as β-actin mRNA in neurons, are known to exist in a masked and translationally inactive state (Buxbaum et al., 2014). Recent work has shown that localized mRNAs are co-transported with membranous compartments, such as those of the ER (Jansen et al., 2014; Schmid et al., 2006). Since the translation of membrane and secreted proteins occurs at the rough ER, the coordination between mRNA localization and ER distribution provides a mechanism behind the local translation of these mRNAs. Future studies will focus on revealing how *Dictyostelium* may use similar mechanisms to mediate ACA mRNA localization and its local translation.

In conclusion, by using the MS2-based live cell imaging system and FRAP analyses, we established that ACA mRNA is transported to the back of polarized chemotaxing cells, where it is actively translated. We envision that *Dictyostelium* cells exploit this mechanism to maintain a polarized distribution of the ACA protein during streaming. As the polarized distribution of many cytoskeletal and signaling components is required during fast chemotactic events, we propose that similar mechanisms are at play in other highly dynamic fast-moving cells, such as immune cells and metastatic cancer cells.

MATERIALS AND METHODS

Plasmids

Plasmids for expression of ACA–YFP–24xMS2, ACA–24xMS2, cAR1–YFP–24xMS2, ACA-2799–24xMS2, ACA-3018–24xMS2 and ACA-3911–24xMS2 were generated using Gateway LR recombination (Thermo Fisher Scientific 11791-100) between pCR8-GW/TOPO (Thermo Fisher Scientific K250020SC) carrying wild-type ACA, ACA–YFP, ACA C-terminal deletion PCR products or cAR1–YFP-coding sequence, and pDM353 vector (Dictybase), which has a 24xMS2 sequence inserted in front of the *actin 8* terminator. The GFP-stop–ACA (or ACA1∼4)–24xMS2 chimeric constructs were generated using Gateway LR recombination between pCR8-GW/TO carrying ACA or ACA1∼4 coding sequence, and pDM351 vector, which had the existing GFP sequence replaced by a GFP with the stop codon 'TAA'. The GFP-stop–24xMS2 construct was generated by removing the LR recombination sequence from the modified pDM351 vector. MS2–mRFPmars was generated by ligating the MS2 PCR product into the pDM451 vector and replacing the hygromycin-resistance gene with the blasticidin-resistance gene. The MS2–mRFPmars–GFP–TubA construct was generated by inserting GFP–TubA-coding sequence (from Dictybase) into the NgoMIV site of the MS2–mRFPmars construct.

Preparation of cells

All cell lines originate from the Parent laboratory. All cells were grown in shaking cultures to ∼4×10^6 cells/ml in HL5 medium (Kriebel et al., 2003). They were harvested by centrifugation (700 ***g*** for 2 min) and washed once in developmental buffer (DB; 5 mM Na_2HPO_4, 5 mM NaH_2PO_4 pH 6.2, 2 mM $MgSO_4$, 200 µM $CaCl_2$). To reach the chemotaxis-competent stage, cells were shaken at 140 rpm for 5.5–7 h with pulses of 75 nM cAMP every 6 min (Devreotes et al., 1987; Parent and Devreotes, 1996). The cells were then processed according to the assay performed.

Lattice light-sheet microscopy

The lattice light-sheet microscope (LLSM) used in these experiments is housed in the Advanced Imaging Center (AIC) at the Howard Hughes Medical Institute Janelia research campus. The system is configured and operated as previously described (Chen et al., 2014). Briefly, chemotaxis-competent *Dictyostelium* cells were spotted on 5-mm round glass coverslips (Warner Instruments, Catalog # CS-5R) and imaged in DB at 22°C. Samples were illuminated by a lattice light-sheet using 488 nm and 560 nm diode lasers (MPB Communications) through an excitation objective (Special Optics, 0.65 NA, 3.74-mm WD). Fluorescence emission was collected by the detection objective (Nikon, CFI Apo LWD 25XW, 1.1 NA), and detected by a sCMOS camera (Hamamatsu Orca Flash 4.0 v2). Acquired data were de-skewed as previously described (Chen et al., 2014) and deconvolved using an iterative Richardson–Lucy algorithm. Point-spread functions for deconvolution were experimentally measured using 200 nm tetraspeck beads adhered to 5-mm glass coverslips (Invitrogen, Catalog # T7280) for each excitation wavelength.

Under-agarose assay

Two-well chamber slides were coated with 1% bovine serum albumin (BSA) in phosphate buffer (PB; 5 mM Na_2HPO_4, 5 mM NaH_2PO_4 pH 6.2) for 1 h at room temperature. 1.2 ml of 0.5% agarose in PB was poured into each well and allowed to solidify for 30 min. Five 1 mm diameter wells were then carved at 2 mm distance from each other. 5 µM cAMP in PB was injected into the center well 5 min before plating cells. 5×10^4 chemotaxis-competent cells in 5 µl PB were then plated in the outer wells. Cells were allowed to chemotax for 30 min to 2 h depending on the experimental requirement. Cells migrating under-agarose were imaged by using a Zeiss LSM 780 laser-scanning confocal microscope (Carl Zeiss, Inc.).

Quantification of the ACA mRNA localization

MS2–RFP-positive cells were recognized and tracked in each frame of every movie. We determined the approximate locations of mRNA spots by setting a threshold that was based on the intensity distribution of the whole cell. After we obtained the approximate localization of mRNA spots, we used an algorithm to calculate the local background by making a 2D plane fit. Finally, the value of the 2D plane was subtracted from the mRNA spot areas to provide the real signal of the mRNA spots. The cell nucleus was identified in the bright-field channel. After tracking every individual cell, coordinates of cell mass centers, instantaneous speed and other information can be obtained. To automatically determine cell front–back polarity, we use five consecutive time points to calculate the average turning angle, and assigned this average turning angle to the center time point as the instantaneous direction of the cell. After rotating the whole cell and normalizing cell lengths according to the speed direction over all time points, we align every individual cell in different frames and make a kymograph for each cell. The kymograph not only shows the asymmetric localization of ACA mRNA granules at cell back, but also allows us to calculate the mRNA SDF across different cells. Adapted from the pair-correlation function in soft matter physics, the mRNA SDF is the probability function that describes the density of fluorescently labeled mRNA signals as a function of the distance from the cell nucleus. To calculate the mRNA SDF, we set the cell nucleus as the origin point and drew a ring with radius r and width Δr. The pixel number of mRNA spots $[n(r \sim r+\Delta r)]$ was counted within the ring and was divided by the product of the ring area ($2\pi r\Delta r$) and the overall mRNA pixel density throughout the whole cell area $[\rho = \frac{n(all\ signal)}{cell\ area}]$. We defined this probability ratio as the mRNA SDF. From the mRNA SDF for each movie, we generated the mRNA SDF for each cell line statistically and compared them between different cell lines.

FRAP analysis

Chemotaxis-competent ACA–YFP/*aca*$^-$ or cAR1–YFP/*car1/3*$^-$ cells were diluted 1:50, spotted onto chamber slides and allowed to adhere for 5 min. Cells were flattened with a 4 mm-thick slice of 0.5% agarose gel in PB so that the entire cell body was within a height that could be visualized and bleached. All the FRAP experiments were performed on a Leica SP8 confocal microscope with 2 AU pin hole. A single section image was taken before bleaching to calculate the starting fluorescence intensity. The bleach region of interest (ROI) was expanded to cover the whole cell. The whole cell was exposed to six iterations of saturating 514 nm, 506 nm, 498 nm, 490 nm and 482 nm laser lines separated from a white laser source. A series of single-plane time-lapse images at 45 s or 50 s intervals were taken using a 63×/1.40 oil HC PL APO CS2 objective. For ACA–YFP/*aca*$^-$ cells, the recovery of fluorescence intensity was measured in three ROIs that include the enrichment of ACA at the back of the cell and the side of the polarized cell membrane, as well as the cell cytosol. All image processing was performed using the LAS X software (Leica Microsystems GmbH). The fluorescence intensity values of each ROI over time were normalized so that the starting value was 100%. The normalized fluorescence recovery of all ROIs were obtained from five independent cells, averaged and plotted over time. For ACA–YFP cell FRAP under PMY treatment, cells were pre-treated with 50 mg/ml PMY for 30 min after 5.5 h development in a shaking flask. Cells were then spotted on chamber slides with the presence of PMY for FRAP experiments. Photobleaching was performed on cAR1–YFP/*car1/3*$^-$, fixed ACA–YFP/*aca*$^-$ and fixed cAR1–YFP/*car1/3*$^-$ cells using the same conditions. However, we only monitored the fluorescence recovery at a single ROI that covers the whole cell. Fluorescence intensity values were obtained, normalized, averaged and graphed as described above.

Ribopuromycylation

Ribopuromycylation was performed as previously described (David et al., 2013, 2012) and modified for *Dictyostelium*. Chemotaxis-competent cells were treated with 50 µg/ml PMY and 208 µM emetine for 10 min at room temperature. All extraction procedures were performed on ice using reagents pre-chilled to 4°C. Cells were incubated for 2 min with 500 µl/well permeabilization buffer [50 mM Tris-HCl pH 7.5, 5 mM $MgCl_2$, 25 mM KCl, 355 µM CHX, EDTA-free protease inhibitors, and 10 U/ml RNaseOut containing 0.015% digitonin (Wako Chemicals)]. After the extraction step, an aliquot was used for western blot analysis. The extracted cells were spun (700 ***g*** for 2 min), resuspended in immunoprecipitation (IP) buffer (40 mM Tris-HCl pH 8.0, 2 mM EDTA, 50 mM NaCl, and 1% CHAPS) and Complete protease inhibitor cocktail (Roche), and solubilized for 1 h on ice. After solubilization, 100 µl of a 50:50 protein A–Sepharose CL-4B (GE Healthcare) and IP buffer slurry was added to each sample, which was incubated on a rotator for 1 h at 4–8°C to preclear the lysate. The protein A–Sepharose was removed by centrifugation and 15 µl of anti-PMY monoclonal antibody (EMD Millipore, MABE343) was added per milliliter of lysate, and incubated on a rotator overnight at 4–8°C. 100 µl of a 50:50 protein A–Sepharose slurry was added and incubated for a further 2 h at 4–8°C to precipitate the puromycylated protein complex. Samples were washed four times with 1 ml IP buffer. The precipitated proteins were released from the Sepharose beads by adding Laemmli buffer and boiling for 10 min. The resulting samples were run using the Criterion gel system (Bio-Rad Laboratories) using a 4–20% Tris-HCl gel, and immunoblotted with anti-rpl8 polyclonal antibody. RNA associated with the immunoprecipitated complex was dissociated with 10 U/ml RNaseOut containing 0.015% digitonin and used in RT-PCR.

Nocodazole and Latrunculin A recovery

Cells were differentiated as described for 5.5 h in shaking flasks containing 2×10^7 cells/ml. At the end of 5.5 h, 15 µM nocodazole or 5 µM Latrunculin A was added to the cells in shaking flask for an additional 1 h to inhibit microtubule or actin polymerization. Cells were then harvested and washed to remove traces of the drug and resuspended in PB. The cells were plated and the recovery of fluorescence was monitored at different time points by imaging using a Zeiss LSM 880 laser-scanning confocal microscope (Carl Zeiss, Inc.).

RNA isolation and analysis

RNA was isolated by using an RNeasy mini plus kit (Qiagen). 1 µg of RNA was reverse transcribed using a High-Capacity cDNA reverse transcription kit (Thermo Fisher Scientific), according to the manufacturer's instructions.

cDNA was used for PCR reactions (details of primer sequences and conditions are available on request).

Antibodies and immunoblotting

Whole-cell lysates were subjected to a 4–20% Tris-HCl SDS-PAGE analysis using the Criterion gel system, and transferred to Immobilon-P (Millipore) membranes. The Immobilon-P membranes were blotted with anti-PMY monoclonal antibody (Millipore, MABE343, 1.66 µg/ml), anti-RPL8 (ARP40215, Aviva Systems Biology, 1:1000) and detection was performed by chemiluminescence using a donkey anti-mouse-IgG horseradish peroxidase (HRP)-coupled antibody (1:5000; GE Healthcare) or an anti-rabbit-IgG horseradish peroxidase-coupled antibody (1:10,000; GE Healthcare) and the ECL Western blotting detection reagents (GE Healthcare). A mouse monoclonal antibody against calnexin was obtained from the Developmental Studies Hybridoma Bank maintained by the Department of Biological Sciences at The University of Iowa (Iowa City, IA) as previously described (Garcia et al., 2009).

Fluorescent *in situ* hybridization

Vegetative or chemotaxis-competent cells were fixed in 3% paraformaldehyde and permeabilized with Triton X-100 (0.1% v/v) in phosphate buffer. A mixture of 48 FISH DNA probes (~22 nt long) was commercially synthesized (Biosearch technologies) and processed according to the manufacturer's protocol. Briefly, fixed cells were hybridized with the FISH probes for 4 h at 37°C in 10% formamide in 2× saline-sodium citrate (SSC) hybridization buffer. The coverslips were washed three times with 2× and 1× SSC buffer, and the nuclei were stained with DAPI. The slides were imaged using a confocal microscope (Zeiss LSM 510 or 780, Carl Zeiss Inc.). Single-plane images and *z*-stacks (1-µm confocal slice) were taken using 63× and 100× plan neofluor objectives (Carl Zeiss, Inc.) and *z*-stacks were presented as maximum intensity projections.

Acknowledgements

We would like to thank Drs Daniel Larson and Stavroula Mili for valuable input and discussions, as well as Dr Jonathan Yewdell for providing the anti-puromycin antibody and for very useful insight. We thank the members of the Parent and Losert laboratory for excellent discussions and suggestions. We thank Susan Garfield, Langston Lim, and Poonam Mannan in the confocal microscopy core of the NCI for the help with imaging. The Advanced Imaging Center is jointly supported by the Howard Hughes Medical Institute and the Gordon and Betty Moore Foundation. We would like to thank Dr John Heddleston and Dr Teng-Leong Chew in the Advanced Imaging Center at Howard Hughes Medical Institute Janelia Farm Research Campus for helping with the lattice light-sheet microscopy experiments.

Competing interests

The authors declare no competing or financial interests.

Author contributions

Conceptualization: W.W., S.C., S.D., C.A.P.; Methodology: W.W., S.C., S.D., W.L., C.A.P.; Software: S.C., W.L.; Validation: W.W.; Formal analysis: W.W., S.C., S.D.; Investigation: W.W., S.C., S.D.; Resources: C.A.P.; Data curation: S.D.; Writing - original draft: W.W., C.A.P.; Writing - review & editing: W.W., S.C., S.D., W.L., C.A.P.; Visualization: W.W., S.C.; Supervision: W.L., C.A.P.; Project administration: C.A.P.; Funding acquisition: W.L., C.A.P.

Funding

This work was supported by the Intramural Research Program of the Center for Cancer Research, National Cancer Institute, National Institutes of Health (to C.A.P.) and by the National Institutes of Health (grant R01GM085574 to W.L.). Deposited in PMC for release after 12 months.

Supplementary information

Supplementary information available online at
http://jcs.biologists.org/lookup/doi/10.1242/jcs.216176.supplemental

References

Anderson, P. and Kedersha, N. (2009). RNA granules: post-transcriptional and epigenetic modulators of gene expression. *Nat. Rev. Mol. Cell Biol.* **10**, 430-436.

Artemenko, Y., Lampert, T. J. and Devreotes, P. N. (2014). Moving towards a paradigm: common mechanisms of chemotactic signaling in Dictyostelium and mammalian leukocytes. *Cell. Mol. Life Sci.* **71**, 3711-3747.

Bassell, G. J., Zhang, H., Byrd, A. L., Femino, A. M., Singer, R. H., Taneja, K. L., Lifshitz, L. M., Herman, I. M. and Kosik, K. S. (1998). Sorting of beta-actin mRNA and protein to neurites and growth cones in culture. *J. Neurosci.* **18**, 251-265.

Beach, D. L., Salmon, E. D. and Bloom, K. (1999). Localization and anchoring of mRNA in budding yeast. *Curr. Biol.* **9**, 569-578.

Bergsten, S. E. and Gavis, E. R. (1999). Role for mRNA localization in translational activation but not spatial restriction of nanos RNA. *Development* **126**, 659-669.

Bertrand, E., Chartrand, P., Schaefer, M., Shenoy, S. M., Singer, R. H. and Long, R. M. (1998). Localization of ASH1 mRNA particles in living yeast. *Mol. Cell* **2**, 437-445.

Buxbaum, A. R., Wu, B. and Singer, R. H. (2014). Single beta-actin mRNA detection in neurons reveals a mechanism for regulating its translatability. *Science* **343**, 419-422.

Buxbaum, A. R., Haimovich, G. and Singer, R. H. (2015). In the right place at the right time: visualizing and understanding mRNA localization. *Nat. Rev. Mol. Cell Biol.* **16**, 95-109.

Chartrand, P., Meng, X.-H., Singer, R. H. and Long, R. M. (1999). Structural elements required for the localization of ASH1 mRNA and of a green fluorescent protein reporter particle in vivo. *Curr. Biol.* **9**, 333-336.

Chen, W., Tan, S. S., Huang, Z. S., Ng, T.-K., Ford, W. T. and Tong, P. (2006). Measured long-ranged attractive interaction between charged polystyrene latex spheres at a water-air interface. *Phys. Rev. E Stat. Nonlin. Soft. Matter Phys.* **74**, 021406.

Chen, B.-C., Legant, W. R., Wang, K., Shao, L., Milkie, D. E., Davidson, M. W., Janetopoulos, C., Wu, X. S., Hammer, J. A., III, Liu, Z. et al. (2014). Lattice light-sheet microscopy: imaging molecules to embryos at high spatiotemporal resolution. *Science* **346**, 1257998.

Chubb, J. R., Trcek, T., Shenoy, S. M. and Singer, R. H. (2006). Transcriptional pulsing of a developmental gene. *Curr. Biol.* **16**, 1018-1025.

Das, S., Parker, J. M., Guven, C., Wang, W., Kriebel, P. W., Losert, W., Larson, D. R. and Parent, C. A. (2017). Adenylyl cyclase mRNA localizes to the posterior of polarized DICTYOSTELIUM cells during chemotaxis. *BMC Cell Biol.* **18**, 23.

David, A., Dolan, B. P., Hickman, H. D., Knowlton, J. J., Clavarino, G., Pierre, P., Bennink, J. R. and Yewdell, J. W. (2012). Nuclear translation visualized by ribosome-bound nascent chain puromycylation. *J. Cell Biol.* **197**, 45-57.

David, A., Bennink, J. R. and Yewdell, J. W. (2013). Emetine optimally facilitates nascent chain puromycylation and potentiates the ribopuromycylation method (RPM) applied to inert cells. *Histochem. Cell Biol.* **139**, 501-504.

Decker, C. J. and Parker, R. (2012). P-bodies and stress granules: possible roles in the control of translation and mRNA degradation. *Cold Spring Harb. Perspect Biol.* **4**, a012286.

Devreotes, P., Fontana, D., Klein, P., Sherring, J. and Theibert, A. (1987). Transmembrane signaling in Dictyostelium. *Methods Cell Biol.* **28**, 299-331.

Firestone, A. J., Weinger, J. S., Maldonado, M., Barlan, K., Langston, L. D., O'Donnell, M., Gelfand, V. I., Kapoor, T. M. and Chen, J. K. (2012). Small-molecule inhibitors of the AAA+ ATPase motor cytoplasmic dynein. *Nature* **484**, 125-129.

Forrest, K. M. and Gavis, E. R. (2003). Live imaging of endogenous RNA reveals a diffusion and entrapment mechanism for nanos mRNA localization in Drosophila. *Curr. Biol.* **13**, 1159-1168.

Fusco, D., Accornero, N., Lavoie, B., Shenoy, S. M., Blanchard, J.-M., Singer, R. H. and Bertrand, E. (2003). Single mRNA molecules demonstrate probabilistic movement in living mammalian cells. *Curr. Biol.* **13**, 161-167.

Garcia, G. L., Rericha, E. C., Heger, C. D., Goldsmith, P. K. and Parent, C. A. (2009). The group migration of Dictyostelium cells is regulated by extracellular chemoattractant degradation. *Mol. Biol. Cell* **20**, 3295-3304.

Gavis, E. R. and Lehmann, R. (1992). Localization of nanos RNA controls embryonic polarity. *Cell* **71**, 301-313.

Golding, I. and Cox, E. C. (2004). RNA dynamics in live Escherichia coli cells. *Proc. Natl. Acad. Sci. USA* **101**, 11310-11315.

Halstead, J. M., Lionnet, T., Wilbertz, J. H., Wippich, F., Ephrussi, A., Singer, R. H. and Chao, J. A. (2015). Translation. An RNA biosensor for imaging the first round of translation from single cells to living animals. *Science* **347**, 1367-1671.

Hirokawa, N., Noda, Y., Tanaka, Y. and Niwa, S. (2009). Kinesin superfamily motor proteins and intracellular transport. *Nat. Rev. Mol. Cell Biol.* **10**, 682-696.

Hotz, M. and Nelson, W. J. (2017). Pumilio-dependent localization of mRNAs at the cell front coordinates multiple pathways required for chemotaxis. *Nat. Commun.* **8**, 1366.

Janicki, S. M., Tsukamoto, T., Salghetti, S. E., Tansey, W. P., Sachidanandam, R., Prasanth, K. V., Ried, T., Shav-Tal, Y., Bertrand, E., Singer, R. H. et al. (2004). From silencing to gene expression: real-time analysis in single cells. *Cell* **116**, 683-698.

Jansen, R.-P., Niessing, D., Baumann, S. and Feldbrügge, M. (2014). mRNA transport meets membrane traffic. *Trends Genet.* **30**, 408-417.

Jaramillo, A. M., Weil, T. T., Goodhouse, J., Gavis, E. R. and Schupbach, T. (2008). The dynamics of fluorescently labeled endogenous gurken mRNA in Drosophila. *J. Cell Sci.* **121**, 887-894.
Jeffery, W. R. (1985). The spatial distribution of maternal mRNA is determined by a cortical cytoskeletal domain in Chaetopterus eggs. *Dev. Biol.* **110**, 217-229.
Jung, H., Gkogkas, C. G., Sonenberg, N. and Holt, C. E. (2014). Remote control of gene function by local translation. *Cell* **157**, 26-40.
Kaplan, B. B., Gioio, A. E., Capano, C. P., Crispino, M. and Giuditta, A. (1992). beta-Actin and beta-Tubulin are components of a heterogeneous mRNA population present in the squid giant axon. *Mol. Cell. Neurosci.* **3**, 133-144.
Katz, Z. B., English, B. P., Lionnet, T., Yoon, Y. J., Monnier, N., Ovryn, B., Bathe, M. and Singer, R. H. (2016). Mapping translation 'hot-spots' in live cells by tracking single molecules of mRNA and ribosomes. *Elife* **5**, e10415.
Kedersha, N., Cho, M. R., Li, W., Yacono, P. W., Chen, S., Gilks, N., Golan, D. E. and Anderson, P. (2000). Dynamic shuttling of TIA-1 accompanies the recruitment of mRNA to mammalian stress granules. *J. Cell Biol.* **151**, 1257-1268.
Kollmar, M. and Glöckner, G. (2003). Identification and phylogenetic analysis of Dictyostelium discoideum kinesin proteins. *BMC Genomics* **4**, 47.
Koonce, M. P., Grissom, P. M. and McIntosh, J. R. (1992). Dynein from Dictyostelium: primary structure comparisons between a cytoplasmic motor enzyme and flagellar dynein. *J. Cell Biol.* **119**, 1597-1604.
Kriebel, P. W. and Parent, C. A. (2004). Adenylyl cyclase expression and regulation during the differentiation of Dictyostelium discoideum. *IUBMB Life* **56**, 541-546.
Kriebel, P. W. and Parent, C. A. (2009). Group migration and signal relay in Dictyostelium. *Methods Mol. Biol.* **571**, 111-124.
Kriebel, P. W., Barr, V. A. and Parent, C. A. (2003). Adenylyl cyclase localization regulates streaming during chemotaxis. *Cell* **112**, 549-560.
Kriebel, P. W., Barr, V. A., Rericha, E. C., Zhang, G. and Parent, C. A. (2008). Collective cell migration requires vesicular trafficking for chemoattractant delivery at the trailing edge. *J. Cell Biol.* **183**, 949-961.
Lionnet, T., Czaplinski, K., Darzacq, X., Shav-Tal, Y., Wells, A. L., Chao, J. A., Park, H. Y., de Turris, V., Lopez-Jones, M. and Singer, R. H. (2011). A transgenic mouse for in vivo detection of endogenous labeled mRNA. *Nat. Methods* **8**, 165-170.
Litman, P., Barg, J. and Ginzburg, I. (1994). Microtubules are involved in the localization of tau mRNA in primary neuronal cell cultures. *Neuron* **13**, 1463-1474.
Liu, G., Grant, W. M., Persky, D., Latham, V. M., Jr, Singer, R. H. and Condeelis, J. (2002). Interactions of elongation factor 1alpha with F-actin and beta-actin mRNA: implications for anchoring mRNA in cell protrusions. *Mol. Biol. Cell* **13**, 579-592.
Long, R. M., Singer, R. H., Meng, X., Gonzalez, I., Nasmyth, K. and Jansen, R. P. (1997). Mating type switching in yeast controlled by asymmetric localization of ASH1 mRNA. *Science* **277**, 383-387.
Loschi, M., Leishman, C. C., Berardone, N. and Boccaccio, G. L. (2009). Dynein and kinesin regulate stress-granule and P-body dynamics. *J. Cell Sci.* **122**, 3973-3982.
Manahan, C. L., Iglesias, P. A., Long, Y. and Devreotes, P. N. (2004). Chemoattractant signaling in dictyostelium discoideum. *Annu. Rev. Cell Dev. Biol.* **20**, 223-253.
Mardakheh, F. K., Paul, A., Kümper, S., Sadok, A., Paterson, H., McCarthy, A., Yuan, Y. and Marshall, C. J. (2015). Global analysis of mRNA, translation, and protein localization: local translation is a key regulator of cell protrusions. *Dev. Cell* **35**, 344-357.
Masaki, N., Fujimoto, K., Honda-Kitahara, M., Hada, E. and Sawai, S. (2013). Robustness of self-organizing chemoattractant field arising from precise pulse induction of its breakdown enzyme: a single-cell level analysis of PDE expression in Dictyostelium. *Biophys. J.* **104**, 1191-1202.
McCann, C. P., Kriebel, P. W., Parent, C. A. and Losert, W. (2010). Cell speed, persistence and information transmission during signal relay and collective migration. *J. Cell Sci.* **123**, 1724-1731.
Mollet, S., Cougot, N., Wilczynska, A., Dautry, F., Kress, M., Bertrand, E. and Weil, D. (2008). Translationally repressed mRNA transiently cycles through stress granules during stress. *Mol. Biol. Cell* **19**, 4469-4479.
Muller-Taubenberger, A., Lupas, A. N., Li, H., Ecke, M., Simmeth, E. and Gerisch, G. (2001). Calreticulin and calnexin in the endoplasmic reticulum are important for phagocytosis. *EMBO J.* **20**, 6772-6782.
Parent, C. A. and Devreotes, P. N. (1996). Constitutively active adenylyl cyclase mutant requires neither G proteins nor cytosolic regulators. *J. Biol. Chem.* **271**, 18333-18336.
Pondel, M. D. and King, M. L. (1988). Localized maternal mRNA related to transforming growth factor beta mRNA is concentrated in a cytokeratin-enriched fraction from Xenopus oocytes. *Proc. Natl. Acad. Sci. USA* **85**, 7612-7616.
Rodriguez, A. J., Shenoy, S. M., Singer, R. H. and Condeelis, J. (2006). Visualization of mRNA translation in living cells. *J. Cell Biol.* **175**, 67-76.
Schmid, M., Jaedicke, A., Du, T.-G. and Jansen, R. P. (2006). Coordination of endoplasmic reticulum and mRNA localization to the yeast bud. *Curr. Biol.* **16**, 1538-1543.
Sundell, C. L. and Singer, R. H. (1991). Requirement of microfilaments in sorting of actin messenger RNA. *Science* **253**, 1275-1277.
Tanenbaum, M. E., Gilbert, L. A., Qi, L. S., Weissman, J. S. and Vale, R. D. (2014). A protein-tagging system for signal amplification in gene expression and fluorescence imaging. *Cell* **159**, 635-646.
Vallee, R. B., Williams, J. C., Varma, D. and Barnhart, L. E. (2004). Dynein: An ancient motor protein involved in multiple modes of transport. *J. Neurobiol.* **58**, 189-200.
Yisraeli, J. K., Sokol, S. and Melton, D. A. (1990). A two-step model for the localization of maternal mRNA in Xenopus oocytes: involvement of microtubules and microfilaments in the translocation and anchoring of Vg1 mRNA. *Development* **108**, 289-298.
Zhang, J., Campbell, R. E., Ting, A. Y. and Tsien, R. Y. (2002). Creating new fluorescent probes for cell biology. *Nat. Rev. Mol. Cell Biol.* **3**, 906-918.

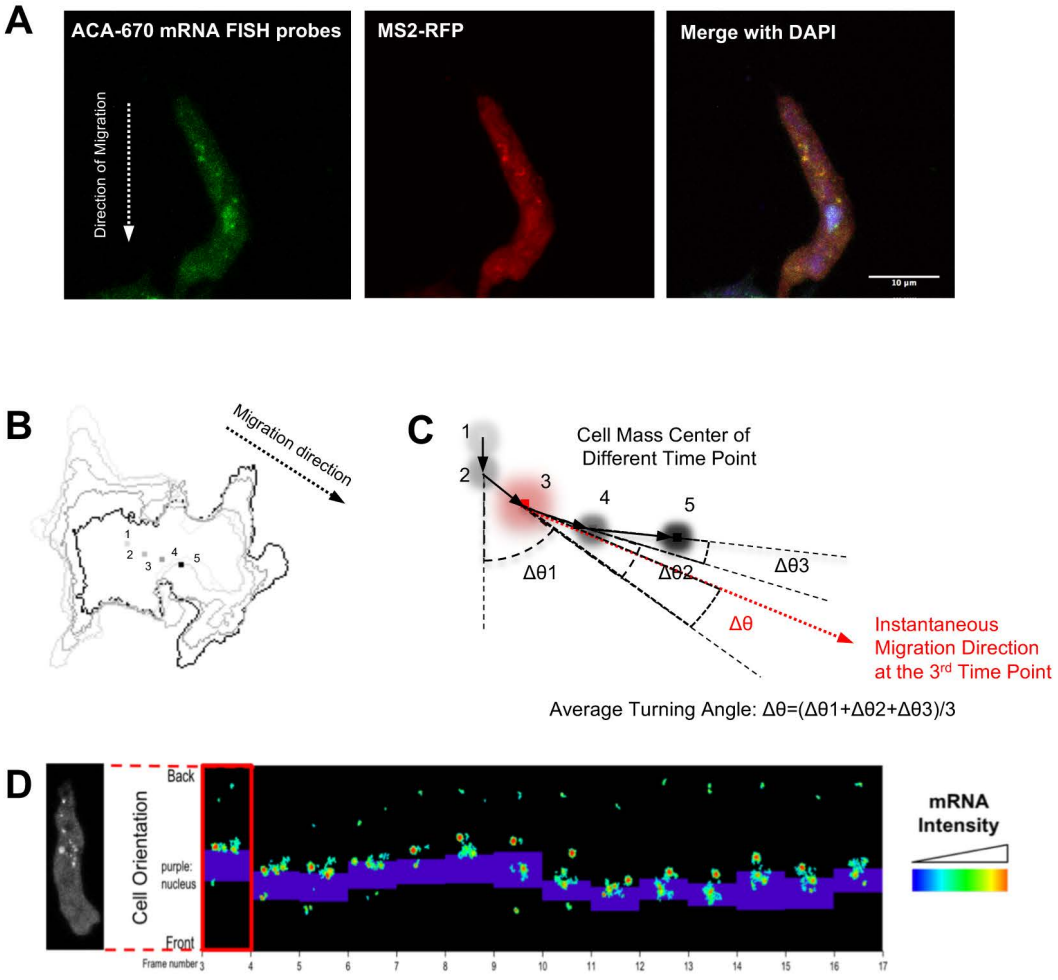

Fig. S1 Live cell ACA mRNA imaging system validation and quantification method
(A) Representative maximum intensity projections of confocal fluorescent images of individual polarized ACA-YFP-24xMS2/MS2-RFP/*aca*$^{-}$ cell depicting ACA mRNA (Green: ACA mRNA FISH probes conjugated with Quasar 670 Dye (Biosearch Technologies); Red: MS2-RFP) and DAPI (Blue).
(B) Representative cell mass center movement in 5 consecutive frames of one movie indicated by numbers. The cell outline in each frame is shown in gradient gray color.
(C) Cell instantaneous migration direction determination.
(D) Kymograph showing the relative ACA mRNA localization in each frame of one movie.

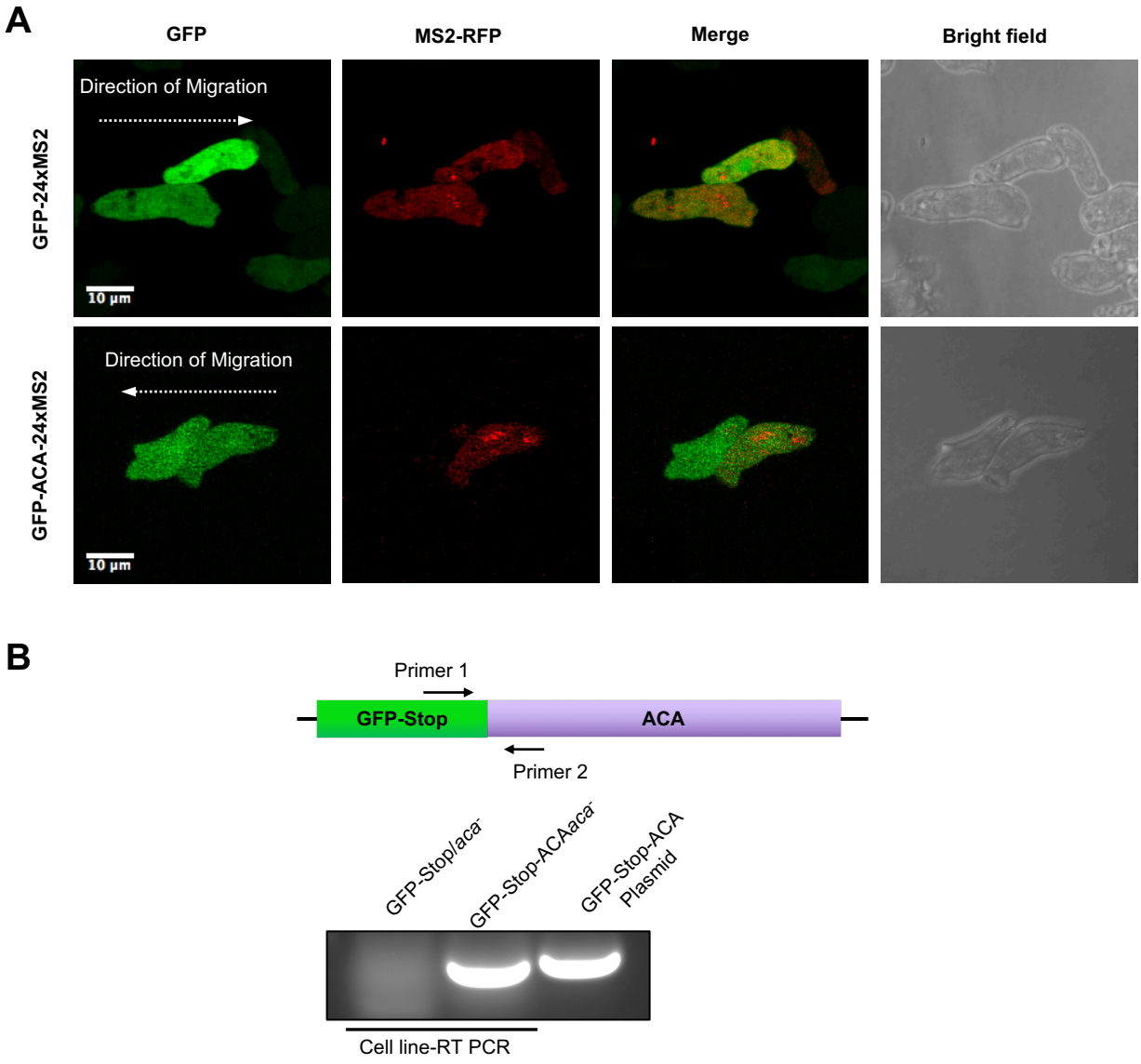

Fig. S2 Expression of chimeric fusion constructs for GFP-24xMS2 and GFP-ACA-24xMS2

(A) Representative maximum intensity projections of GFP-24xMS2/MS2-RFP/*aca*$^-$ and GFP-ACA-24xMS2/MS2-RFP/*aca*$^-$ cells as indicated.

(B) Top panel: Sheme representing primer locations against GFP-ACA construct. Bottom panel: RT-PCR results of mRNA extracted from cell lines and DNA plasmid as indicated using the primer pair in the top panel.

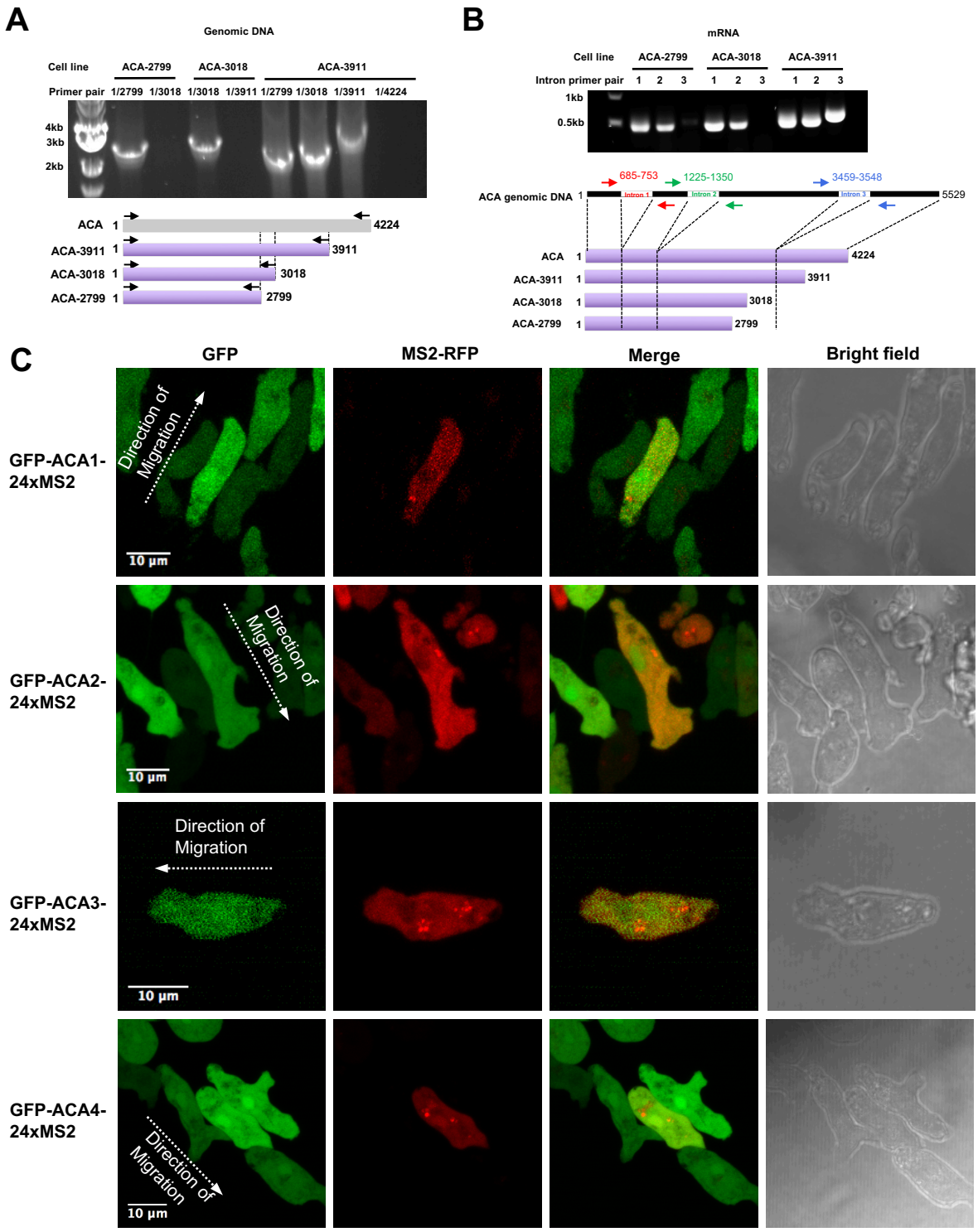

Fig. S3 Expression of chimeric fusion constructs for ACA deletion mutants
(A) PCR results of genomic DNAs from the cells indicated using the primer pairs depicted in the bottom panel.
(B) RT-PCR results of mRNA from the cells indicated using the primer pairs depicted in the bottom panel.
(C) Representative maximum intensity projections of GFP-ACA1~4/MS2-RFP/*aca*$^{-}$ cells as indicated.

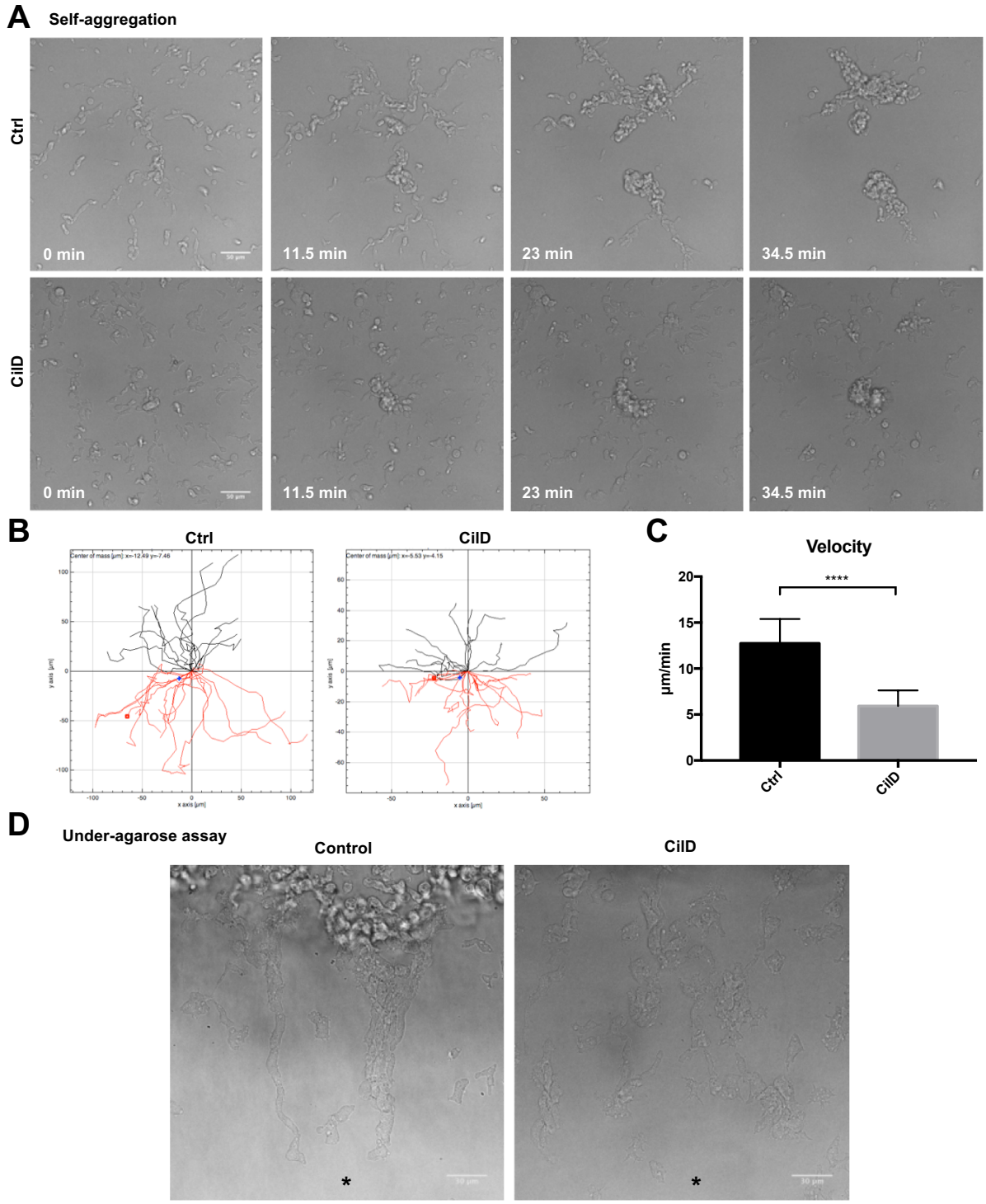

Fig. S4 CilD abolishes streaming and decreases the cell migration speed
(A) Sequential bright field images of control and 40 µM CilD-treated ACA-YFP/*aca*$^{-}$ cells under self-aggregation.
(B) Plots showing the tracks of cell migration in (A) (n=25).
(C) Velocity of the cell migration in (A) (n=25).
(D) Bright field image of control and 40 µM CilD treated ACA-YFP/*aca*$^{-}$ cells chemotaxing towards a gradient of cAMP.

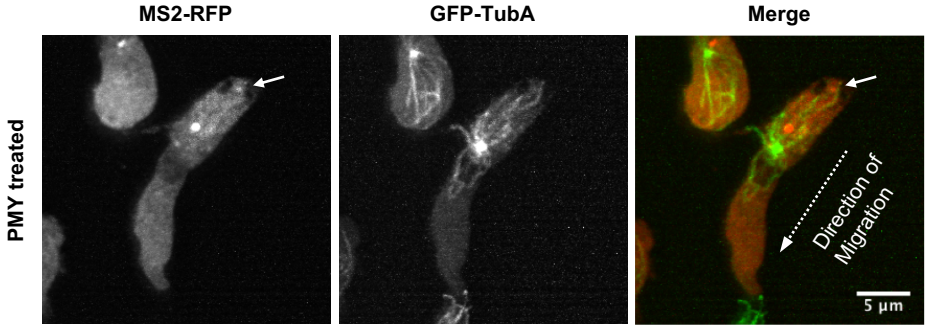

Fig. S5 ACA mRNA remains at the cell back under PMY treatment
Representative maximum intensity projection image of ACA-24xMS2/MS2-RFP/aca- cells migrate on glass coverslip taken by lattice light-sheet microscope. Left: MS2-RFP; center: GFP-TubA; right: merge.

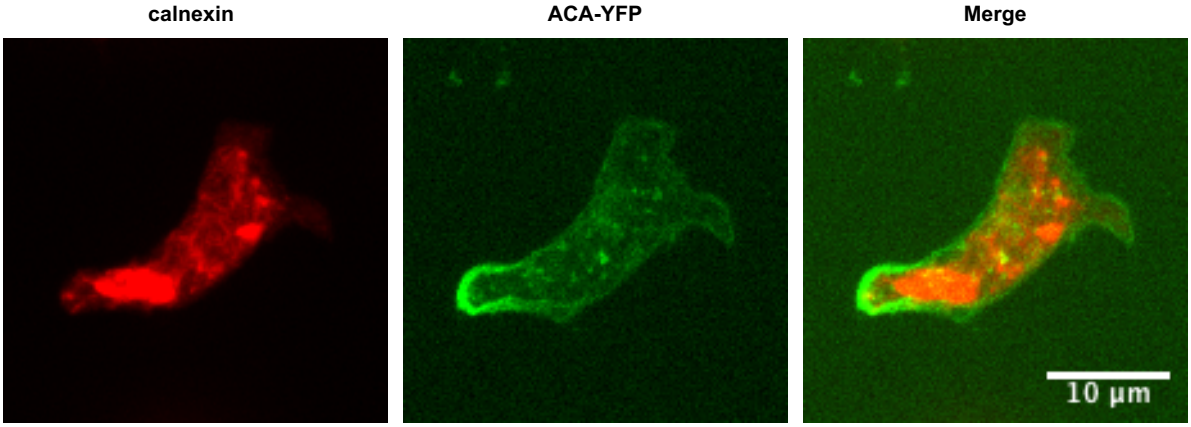

Fig. S6 ER distribution in ACA-YFP/*aca*$^{-}$ cell
Representative maximum intensity projection image of ACA-YFP/aca- cell stained with calnexin.

SUPPLEMENTAL MOVIES

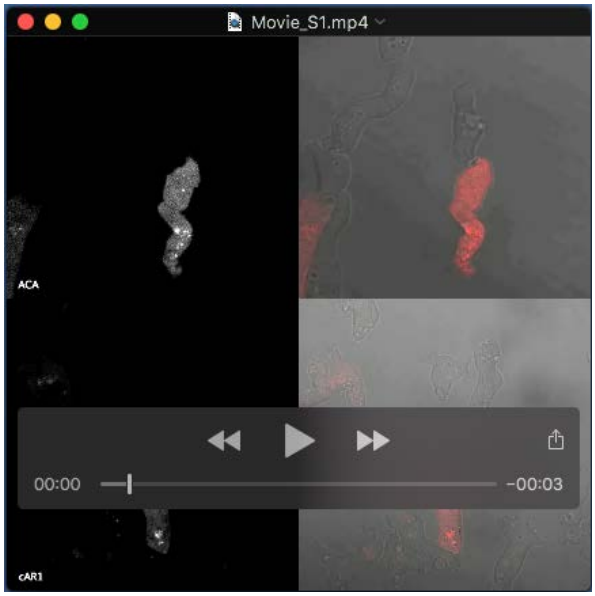

Movie S1. Maximum intensity projection time-lapse images of ACA-YFP-24xMS2/MS2-RFP/*aca*$^{-}$ cells and cAR1-YFP-24xMS2/MS2-RFP/*car1/3*$^{-/-}$ cells - Related to Figure 1.
ACA-YFP-24xMS2/MS2-RFP/*aca*$^{-}$ (top) and cAR1-YFP-24xMS2/MS2-RFP/*car1/3*$^{-/-}$ (bottom) cells migrating towards a cAMP source under agarose. Left: MS2-RFP; Right: Merge with bright field. Images were taken every 15 s and presented at 3 frames/s (fps).

Movie S2. Maximum intensity projection time-lapse images of GFP-24xMS2/MS2-RFP/*aca*$^{-}$ and GFP-ACA-24xMS2/MS2-RFP/*aca*$^{-}$ cells - Related to Figure 2.
GFP-24xMS2/MS2-RFP/*aca*$^{-}$ (top) and GFP-ACA-24xMS2/MS2-RFP/*aca*$^{-}$ (bottom) cells migrating towards a cAMP source under agarose. Left: MS2-RFP; Right: Merge with bright field. Images were taken every 15 s and presented at 7 fps.

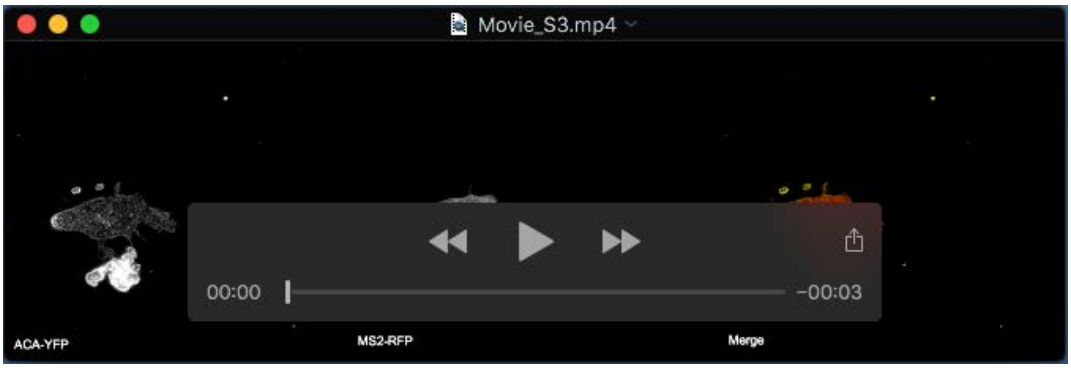

Movie S3. Maximum intensity projection time-lapse images of a ACA-YFP-24xMS2/MS2-RFP/*aca*$^{-}$ cell - Related to Figure 2.

An ACA-YFP-24xMS2/MS2-RFP/*aca*$^{-}$ cell migrating towards a cAMP source under agarose. Left: ACA-YFP; Center: MS2-RFP; Right: Merge. Images were taken every 15 s and presented at 3 fps.

Movie S4. Maximum intensity projection time-lapse images of ACA-2799-24xMS2/MS2-RFP/*aca*$^{-}$, ACA-3018-24xMS2/MS2-RFP/*aca*$^{-}$, and ACA-3911-24xMS2/MS2-RFP/*aca*$^{-}$ cells - Related to Figure 3.

ACA-2799-24xMS2/MS2-RFP/*aca*$^{-}$ (left), ACA-3018-24xMS2/MS2-RFP/*aca*$^{-}$ (center) and ACA-3911-24xMS2/MS2-RFP/*aca*$^{-}$ (right) cells migrating towards a cAMP source under agarose. Images are showing MS2-RFP only. Images were taken every 15 s and presented at 6 fps.

Journal of Cell Science • Supplementary information

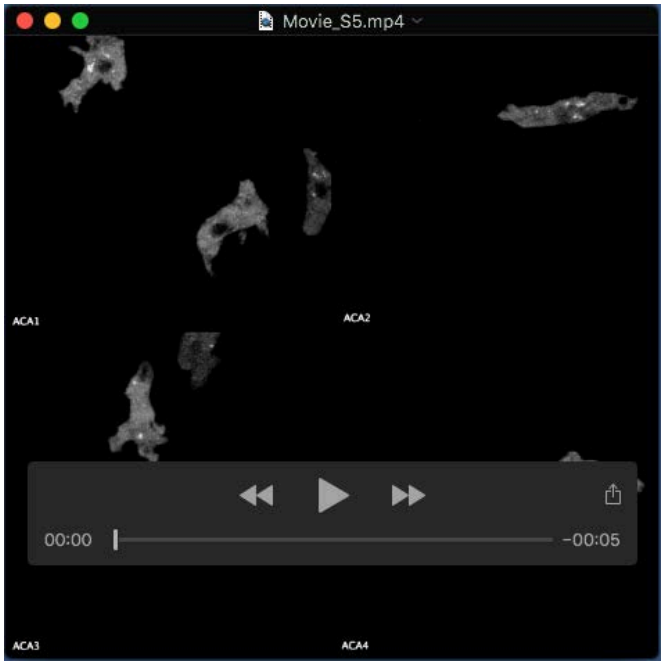

Movie S5. Maximum intensity projection time-lapse images of GFP-ACA1~4-24xMS2/MS2-RFP/*aca*⁻ cells - Related to Figure 3.

GFP-ACA1~4-24xMS2/MS2-RFP/*aca*⁻ (ACA1~4 as depicted) cells migrating towards a cAMP source under agarose. Images are showing MS2-RFP only. Images were taken every 15 s and presented at 6 fps.

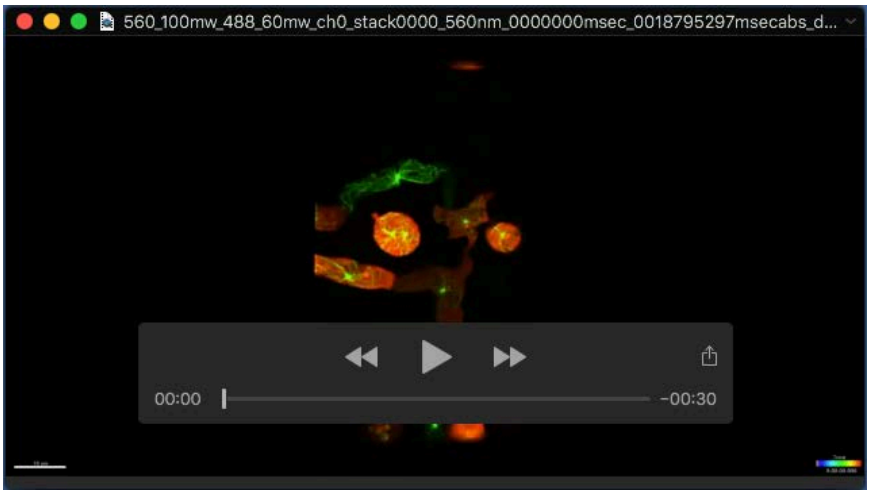

Movie S6. Three-dimensional lattice light-sheet microscopy time-lapse images of ACA-24xMS2/MS2-RFP/GFP-TubA/*aca*⁻ cells - Related to Figure 4.

ACA-24xMS2/MS2-RFP/GFP-TubA/*aca*⁻ cells streaming and self-aggregating on a glass coverslip. Red: MS2-RFP; Green: GFP-TubA. Images were presented at 10 fps.

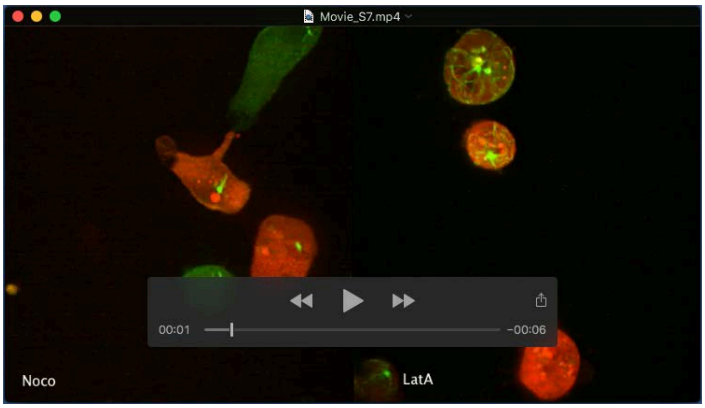

Movie S7. Maximum intensity projection time-lapse images acquired using lattice light-sheet microscopy of ACA-24xMS2/MS2-RFP/GFP-TubA/*aca*$^{-}$ cells treated with Noco (left) and LatA (Right)- Related to Figure 5.

ACA-24xMS2/MS2-RFP/GFP-TubA/*aca*$^{-}$ cells treated with Noco or LatA migrating on a glass coverslip. Red: MS2-RFP; Green: GFP-TubA. Images were presented at 7 fps.

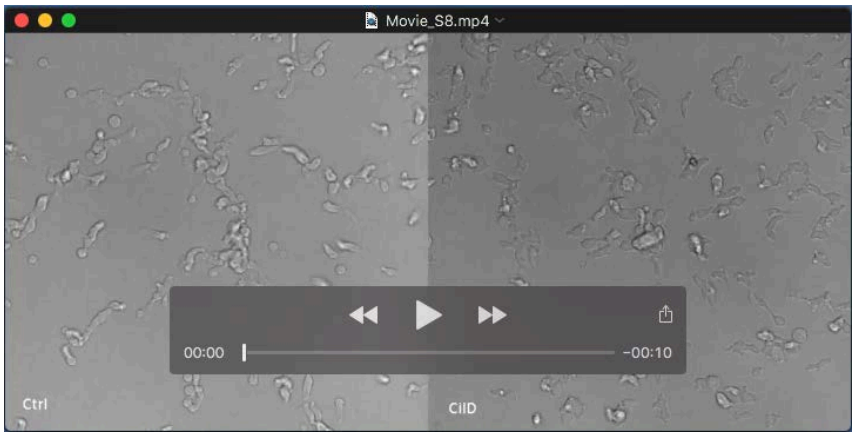

Movie S8. Time-lapse images of ACA-YFP/*aca*$^{-}$ cells self-aggregating in the presence and absence of CilD - Related to Figure 5.

ACA-YFP/*aca*$^{-}$ cells were treated with CilD and allowed to self-aggregate on glass. Images were taken every 30 s and presented at 7 fps.

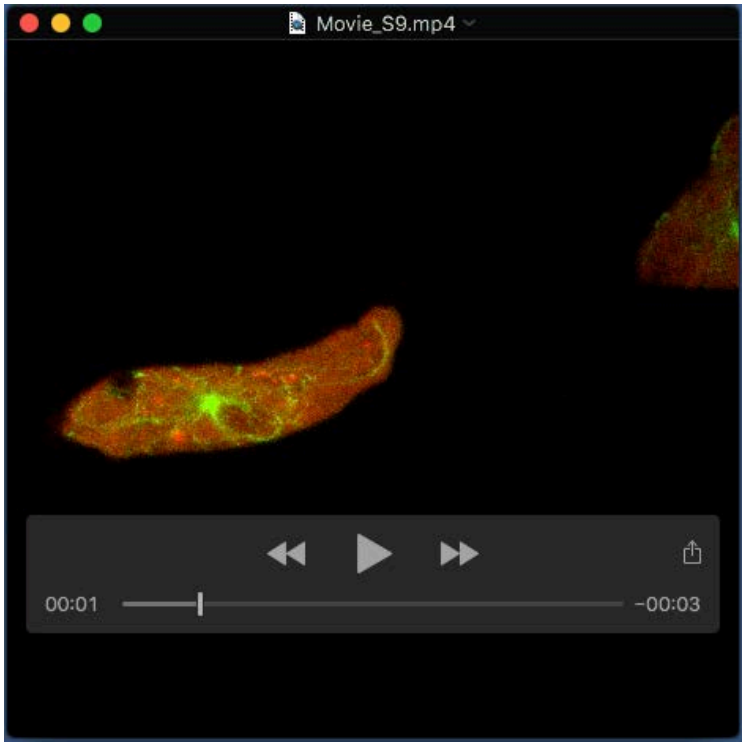

Movie S9. Maximum intensity projection time-lapse images of ACA-24xMS2/MS2-RFP/GFP-TubA/*aca*$^{-}$ cells treated with CilD - Related to Figure 5.

ACA-24xMS2/MS2-RFP/GFP-TubA/*aca*$^{-}$ cell migrating towards a cAMP source under agarose. Red: MS2-RFP; Green: GFP-TubA. Images were taken every 15 s and presented at 4 fps.